Deep vs. shallow origin of gravity anomalies, topography and volcanism on Earth, Venus and Mars

Bernhard Steinberger[a,b,c], Stephanie C. Werner[c] and Trond H. Torsvik[a,c,d]
[a] Center for Geodynamics, Geological Survey of Norway,
NO-7491 Trondheim, Norway
[b] Helmholtz Centre Potsdam, German Research Centre for Geosciences,
Telegrafenberg, 14473 Potsdam, Germany
E-mail: bstein@gfz-potsdam.de; Phone:+49-331-288-1881; Fax:+49-331-288-1938
[c] Physics of Geological Processes, Univ. of Oslo, NO-0316 Oslo, Norway
[d] School of Geosciences, Univ. of the Witwatersrand, Wits 2050, South Africa

34 manuscript pages, 10 figures, 1 table

Proposed running head:

GRAVITY, TOPOGRAPHY, VOLCANISM ON EARTH, VENUS, MARS

editorial correspondence and proofs should be directed to:
Bernhard Steinberger
Center for Geodynamics
Geological Survey of Norway
7491 Trondheim
Norway
e-mail: bernhard.steinberger@ngu.no

ABSTRACT

The relation between gravity anomalies, topography and volcanism can yield important insights about the internal dynamics of planets. From the power spectra of gravity and topography on Earth, Venus and Mars we infer that gravity anomalies have likely predominantly sources below the lithosphere up to about spherical harmonic degree $l = 30$ for Earth, 40 for Venus and 5 for Mars. To interpret the low-degree part of the gravity spectrum in terms of possible sublithospheric density anomalies we derive radial mantle viscosity profiles consistent with mineral physics. For these viscosity profiles we then compute gravity and topography kernels, which indicate how much gravity anomaly and how much topography is caused by a density anomaly at a given depth. With these kernels, we firstly compute an expected gravity-topography ratio. Good agreement with the observed ratio indicates that for Venus, in contrast to Earth and Mars, long-wavelength topography is largely dynamically supported from the sublithospheric mantle. Secondly, we combine an empirical power spectrum of density anomalies inferred from seismic tomography in Earth's mantle with gravity kernels to model the gravity power spectrum. We find a good match between modeled and observed gravity power spectrum for all three planets, except for $2 \leq l \leq 4$ on Venus. Density anomalies in the Venusian mantle for these low degrees thus appear to be very small. We combine gravity kernels and the gravity field to derive radially averaged density anomaly models for the Martian and Venusian mantles. Gravity kernels for $l \geq 5$ are very small on Venus below $\approx$ 800 km depth. Thus our inferences on Venusian mantle density are basically restricted to the upper 800 km. On Mars, gravity anomalies for $2 \leq l \leq 5$ may originate from density anomalies anywhere within its mantle. For Mars as for Earth, inferred density anomalies are dominated by $l = 2$ structure, but we cannot infer whether there are features in the lowermost mantle of Mars that correspond to Earth's Large Low Shear Velocity Provinces (LLSVPs). We find that volcanism on Mars tends to occur primarily in regions above inferred low mantle density, but our model cannot distinguish whether or not there is a Martian analog for the finding that Earth's Large Igneous Provinces mainly originate above the margins of LLSVPs.

Keywords: Earth; Venus, Interior; Mars, Interior; Volcanism

1 Introduction

Gravity anomalies and topography, as well as the distribution of volcanism in space and time, can yield important insights into the internal structure and dynamics of the Earth and planets. For the Earth, we have additional information, most importantly, from seismic tomography. Models derived for the Earth interior, based on the comparatively large amount of information available, can be adapted to other planets. Such models may or may not explain data available for other planets, and thus point towards similarities or differences between the Earth and other planets, and help to shed further light on internal structure and dynamics. Our comparative study includes Earth, Venus and Mars, because Venus is similar in size to Earth, but Venus appears to have a rigid lithosphere rather than featuring plate tectonics, whereas Mars is similar to Venus in terms of having a rigid lid, but different in size. For all three planets, we know the gravity field and topography in great detail, and have abundant information on where and when (less precise for Mars and Venus) volcanic activity occurred.

It is generally agreed upon that planetary interiors are heated through the decay of radioactive nuclides, the heat is released through thermal or thermo-chemical convection combined with conduction through boundary layers, and planetary mantles convect although they are mostly solid: A standard modeling approach is to treat planetary mantles as highly viscous (typically around 10^{21} Pas, with large variations) – at least below the uppermost layer, the lithosphere, which is brittle and where a viscous rheology is therefore inappropriate. Hot and less dense material rises, whereas cold and denser material sinks. For Earth, the lithosphere is broken into $\approx$ a dozen tectonic plates, and the subduction of tectonic plates (mostly oceanic) therefore constitutes the most important part of the downward flow. An endothermic phase transition, which occurs in Earth at depth ≈ 670 km complicates subduction, in that it is believed that only in some places, lithosphere sinks straight towards the base of the mantle (Fukao et al., 2001). On other planets, lithosphere is not at all or only episodically subducted, such that downward flow must take another form.

Upward flow may be in the form of large-scale broad upwellings, or narrow plumes rising through the mantle. Both broad large-scale upwellings – on the Earth for example thought to occur beneath East Africa and the Central Pacific – and narrow plumes – beneath "hotspots", for example Hawaii, have been associated with intra-plate volcanism on Earth and volcanism on other planets. The most prominent form of (mostly intra-plate) volcanism on Earth are Large Igneous Provinces (LIPs), thought to occur when a large plume head impinges upon the lithosphere. Other forms of volcanism on Earth occur along plate boundaries – spreading ridges and subduction zones – and therefore presumably have no equivalent on other planets, whereas some volcanism on other planets is thought to be impact related and thus probably has no equivalent on Earth. Neither for Earth nor other planets, it is generally agreed upon whether upwellings are broad, or narrow plumes, or perhaps a combination of both. The case for mantle plumes is e.g. made by Davies (2005), while alternative but unlikely "shallow" plate tectonic driven mechanisms for LIPs, hotspot and other intra-plate volcanism have also been proposed (e.g. Anderson, 2000).

Finding relations between volcanism and deep mantle features is therefore important in distinguishing deep vs. shallow origin. On Earth, anomalies of seismic velocity are found through seismic tomography. These anomalies are believed, to a large part, to be related to temperature and hence thermal density variations. Compositional variations are believed to contribute to seismic anomalies mainly in the uppermost mantle (lithosphere) and lowermost mantle (D" layer). The most prominent features of all recent tomography models are the Large Low Shear Velocity Provinces (LLSVPs) of the lowermost mantle beneath Africa and the Pacific. When LIPs of the past 300 Myrs are reconstructed to their eruption locations, using models of plate motion relative to the mantle beneath, they tend to cluster over the margins of the LLSVPs (Torsvik et al., 2006). This relation supports both the deep origin of LIPs and and the long-term stability (up to 300 Myrs or longer) and hence presumably chemically distinct nature of LLSVPs.

Whether or not a similar relationship can be found for other planets can hence tell us something about the causes of volcanism on those. In the absence of plate tectonics, we can directly use present-day locations of volcanics instead of having to reconstruct their eruption locations, unless there is a coherent rotation of the entire lithosphere over the deeper mantle ("mantle roll"). However, in the absence of seismic tomography, we need to infer their deep mantle structure mostly based on gravity anomalies or equipotential surface (note that free-air gravity anomaly and equipotential surface are essentially equivalent descriptions, as they are derived from the same set of spherical harmonic coefficients) and possibly surface topography. This certainly leaves us with a much more "blurred" and non-unique picture of planetary mantles. As explained in the following, we believe that we can get the most information by considering gravity (and possibly topography) in both the space and spectral domain:

Considering the space domain, large-scale geoid highs on Earth appear to approximately correspond to LLSVPs (Burke et al., 2008), and in particular if those parts of the geoid caused by subducted slabs are taken away (Hager, 1984). We can therefore, as a first approximation, assume that highs of the equipotential surface (geoid on Earth, areoid on Mars, aphroditoid on Venus – we will henceforth, for the sake of convenience, refer to all three of them as "geoid" despite the linguistic inconsistency) overly LLSVPs or equivalent features.

However, the relation between geoid and density heterogeneities in a convecting mantle is not straightforward: A negative density anomaly by itself causes a negative gravity anomaly and geoid low, but the viscous flow driven by it also causes upward deflection of the top surface and core-mantle boundary (CMB), which, in turn, contributes a positive gravity anomaly and geoid high. Thus, in combination, a negative density anomaly may be associated with either a geoid high or low, and the resulting geoid critically depends on mantle viscosity structure. For Earth, it has been shown that, with an appropriate mantle viscosity structure the large-scale geoid can to a large part be explained as caused by mantle density anomalies (derived from seismic tomography) and the flow and boundary (surface and CMB) deformation they cause (e.g., Hager and Richards, 1989). We can then attempt to "translate" best-fitting viscosity-depth profiles from the Earth to other planets, considering the different profiles of temperature and pressure versus depth. With these translated profiles, we can investigate which mantle density anomalies are compatible with the observed gravity anomalies and topography.

Considering the spectral domain, it has been shown for Earth that, with the same viscosity models, the shape of the gravity spectrum (Steinberger and Holme, 2002) can be explained based on mantle density anomalies. Importantly, it can be even better explained if, instead of using density anomalies based on tomography, a simple model of random density anomalies, with only its spectral characteristics inferred from tomography, is used. For Earth, this explanation works up to about degree $l = 31$. For shorter wavelengths, gravity is presumably dominated by lithospheric contributions. As an additional consistency check we can therefore use the viscosity and spectral density models, translated to the other planets, to compute gravity and topography spectra. Whether, and if so, in what degree range, observed and modeled gravity and topography spectra agree within uncertainties, can then give a further indication whether the viscosity profile is appropriate, which part of the spectra may be caused by density anomalies in the mantle beneath the lithosphere, and which parts are primarily caused from within the lithosphere. This question has been addressed in a number of recent papers. Kiefer et al. (1996) found that the Martian geoid up to degree 10 and topography up to degree 3 is predominantly caused by mantle thermal structure, but studies of the Tharsis rise on Mars implied that it is caused either predominantly or wholly by surface loading and at most a smaller contribution from internal loading (Lowry and

Zhong, 2003; Roberts and Zhong, 2004; Redmond and King, 2004).

This paper therefore consists of the following parts: In section 2 we introduce our data sources for gravity and topography and respective spectra. We also discuss here, based on spectral characteristics, which part of the spectrum may have possibly a sublithospheric origin and is therefore further considered in the paper. In section 3, we derive radial profiles for density, gravity, pressure, temperature and viscosity, and hence infer the relation between density anomalies, gravity and (dynamic) topography. In section 4, we compare predicted and observed spectra for gravity and topography for the Earth, Venus and Mars and thus infer which part of the spectra is likely caused by sub-lithospheric mantle density anomalies, and we use these results to derive tentative models of mantle density anomalies for Mars and Venus. Finally, in chapter 5, we discuss our results – in particular, the implications with respect to relating mantle density anomalies to volcanism.

2 Gravity and topography of Earth, Venus and Mars: Data and spectral characteristics

Gravity and topography of Earth, Venus and Mars are known very well and to a high spherical harmonic degree. We shall use here some of the most up-to-date models available:

We use geopotential model ITG-Grace03 (Mayer-Gürr et al, 2007) for Earth, and gravity models SHGJ180U.A01 (Konopliv, 2006) for Venus, and JGM95J01 and JGM85F02 (Konopliv et al., 2006), online at http://pds-geosciences.wustl.edu/geodata/mgs-m-rss-5-sdp-v1/mors_1033/sha/jgm95j01.SHA and http://www.igpp.ucla.edu/cache1/MORS_1024/SHA/JGM85F02.SHA for Mars. Topography is obtained from the shapes of Earth, Venus and Mars as given by Wieczorek (2007), online at http://www.ipgp.jussieu.fr/∼wieczor/SH/SH.html. All these models are given in terms of fully normalized spherical harmonic expansion coefficients $\bar{C}_l^m$ and $\bar{S}_l^m$ of the gravity potential, normalized through dividing by GM_0/r_0, where G is the gravitational constant, M_0 is planetary mass and r_0 is the planetary mean radius (for details, see e.g. Stacey, 1977).

For a meaningful geodynamic interpretation, the equipotential surface should be relative to the hydrostatic equilibrium shape (Clairaut, 1743), and topography relative to the equipotential surface. For Earth, we use the equilibrium shape of Nakiboglu (1982). Thus, the coefficient $\bar{C}_2^0$ of the ITG-Grace03 model is replaced by $\bar{C}_{2,ne}^0 = \bar{C}_2^0 - \bar{C}_{2,eq}^0$ whereby *eq* indicates "equilibrium" *ne* indicates “non-equilibrium”; $\bar{C}_4^0$ is replaced by $\bar{C}_{4,ne}^0$. Coefficients are listed in Table 1. $\bar{C}_6^0$ and $\bar{C}_8^0$ are not modified here, because the corresponding coefficients of the reference shape are small in comparision, hence we expect the same for the equilibrium shape.

For Venus, the modification of all coefficients is very small, compared to the coefficents themselves, due to its slow rotation rate. Therefore, none of the coefficients are modified for Venus.

For Mars, equilibrium flattening is computed based on the density profiles derived in the next section with a first order accurate algorithm (Steinberger, 1996). From this, equilibrium and non-equilibrium potential coefficients (Table 1) are obtained with the second-order equations given by Stacey (1977, p. 55) To test the algorithm, we also computed equilibrium flattening of the Earth for the PREM (Dziewonski and Anderson, 1981) density profile. We obtained a value 1/299.90, corresponding to a $\bar{C}_{2,eq}^0$ coefficient that differs from the one computed by Nakiboglu (1982) with second-order theory by 0.2 %. The flattening obtained for Mars is also similar, though not identical to the result of Sleep and Phillips (1985).

Table 1

We note, though, that the equilibrium shape of Mars is subject to uncertainties. Dadarich et al. (2008) point out that the result changes if a lithosphere with long-term elastic strength is considered. We also note that, for the present Martian rotation axis to be stable, relative to the Martian mantle (i.e. correspond to the maximum non-hydrostatic moment of inertia) it is required that $\bar{C}_{2,ne}^0 < -\sqrt{(\bar{C}_2^{2\;2} + \bar{S}_2^{2\;2})/3} = -56.4 \cdot 10^{-6}$ and our above-derived value satisfies this condition.

Topography coefficients are obtained by subtracting expansion coefficients of the equipotential surface from those of the shape. For the Earth’s shape, we use the model where the ocean mass has been converted to ”rock equivalent topography” by adding 1030/2670 of the ocean depths. The equipotential surface is obtained from the sum of gravity potential and rotational potential. The latter affects only the expansion coefficients for degree zero and degree two order zero. For Venus, rotational potential is already included in the gravity model (Wieczorek, 2007), thus coefficients are not modified. For Mars, we use here gravity model JGM95J01. As in Steinberger and Holme (2002) we follow Hipkin (2001) for definition of the power spectrum, except for an additional factor r_0^2: We define average gravity power $\langle P_l \rangle$ of each spherical harmonic component of degree l as

$$\langle P_l \rangle = r_0^2 \cdot (l+1) \left(\bar{C}_l^{0\;2} + \sum_{m=1}^{l} (\bar{C}_l^{m\;2} + \bar{S}_l^{m\;2}) \right) \qquad (1)$$

because $\sqrt{\langle P_l \rangle}$ is then in units of meters, thus corresponding to deflection of the equipotential surface, i.e. geoid anomalies.

We restrict our analysis to spherical harmonic degrees $2 \leq l \leq 95$, as Martian gravity is only expanded to degree 95, and any sub-lithospheric gravity contribution at degrees $l > 95$ is almost certainly negligible. In order to determine which parts of the gravity spectrum for Earth, Venus and Mars are of possibly of deep (i.e., sub-lithospheric) origin, we analyse the spectra in the following way:

We "downward-continue" the spectra to a depth d by multiplying power for degree l with $[r_0/(r_0 - d)]^{2l}$. This is merely a matter of presentation, as physically, gravity cannot be downward-continued through the source. We choose d such that the spectrum becomes approximately "white", i.e. flat, between certain l_0 and $l_{\max}$ (= 95 for Earth and Venus, less for Mars – see below). We find that appropriate values are $d = 50$ km for both Earth and Venus and $d = 120$ km for Mars. Results shown in Figs. 1 – 3 indicate $l_0 \approx 31$ for the Earth, $l_0 \approx 40$ for Venus and $l_0 \approx 6$ for Mars. Our first indication is thus that the gravity signal for $l < l_0$ may be of possibly sublithospheric origin, and the signal for $l \geq l_0$ is of mainly lithospheric origin. This is an empirical result, as there is no strict physical base as to why the downward-continued lithospheric power spectrum defined in this way should be "white". However, the following points speak in favour of this assumption:

Firstly, the assumption works very well, at least for the Earth and Venus, with fluctuations approximately as expected for "random" coefficients (by a factor $\approx 1/\sqrt{2l+1}$ as there are 2l+1 coefficients of degree l). For Mars, visual inspection indicates some more structure in the spectrum. Downward-continued spectra appear to increase with l above about degree $l_{\max} = 60$ for the older model JGM85F02 and above about degree $l_{\max} = 80$ for the newer model JGM95J01. The fact that the two models start to visibly disagree above about degree 60, together with the decorrelation of gravity and topography above about degree 60 (discussed below) possibly indicates that this increase is a model artifact rather than a true feature of the gravity field. The issue that higher degrees (above about 70) are less well determined is also discussed by Konopliv et al. (2006).

Secondly, the inferred lithosphere (thermal) thicknesses $2d$ are quite reasonable. For Earth, various lines of evidence suggest an average lithosphere thickness of about 100 km – thicker for continents, thinner for young ocean floor and about 100 km for old ocean floor. For Venus, which is approximately the same size, the same value is found. Here, geologic evidence suggest a rather young (few 100 Ma) surface, consistent with a thin lithosphere. The value 100 km is also consistent with other estimates. Simons et al. (1997) state that a 45- to 150-km-thick thermal boundary layer cannot be rejected on the basis of current geophysical understanding. According to Phillips et al. (1997) stagnant lid parametrized convection solutions produce earthlike lithosphere thicknesses of about 120 km. Mars is smaller and therefore expected to have lost more of its heat. Geologic evidence implies here a surface that is very old in many places – coming close to the age of the planet. Therefore, a substantially thicker lithosphere – as inferred here – is expected.

We now further corroborate this result through testing which part of the gravity field is explained well as caused by topography. Hereby we test the following two assumptions:

1. Topography is isostatically compensated through crustal thickness variations: For a mean crustal thickness t_c the ratio to convert topography to gravity expansion coefficients is then approximately
$$\mathrm{Q}_c = \frac{3}{2l+1}\frac{\rho_c - \rho_a}{\rho_0} \cdot (1 - (1 - t_c/r_0)^l) \tag{2}$$
whereby $\rho_c - \rho_a$ is the density contrast at the solid surface between crustal density ρ_c and atmosphere density ρ_a and ρ_0 is the planetary mean density. Since in case of the Earth we use "rock equivalent" topography, $\rho_c - \rho_a$ should also be approximately the appropriate density contrast. ρ_a is negligible for Earth and Mars. We adjust ρ_c and t_c such as to optimize the fit between modelled and observed gravity spectrum. Varying ρ_c just shifts the modelled spectrum up and down, whereas varying t_c changes its degree dependence.

2. Topography causes deflection of an elastic lithosphere. With topography uncompensated in the limit of very short wavelengths and fully compensated in the limit of very long wavelengths, and the transition occurring at around spherical harmonic degree l_e, the ratio between gravity and topography coefficients should be approximately
$$\mathrm{Q}_e = \frac{3}{2l+1}\frac{\Delta\rho}{\rho_0} \cdot (1 - (1 - t_l/r_0)^l \cdot \Gamma_l) \tag{3}$$

In this case, we take for the compensation depth t_l the above estimate of lithosphere thickness $2d$. The factor Γ_l is the "degree of compensation" for degree l as given by Turcotte et al. (1981), eqn. 27, which accounts for the role of both membrane stresses and bending stresses in supporting topographic loads. In the case of Earth and Venus, membrane stresses are negligible and the expression $\Gamma_l = 1/(1 + l^4/l_e^4)$ can be used (McKenzie and Fairhead, 1997). However, Turcotte et al. (1981) have shown that in the case of Mars membrane stresses cannot be neglected, and one cannot express Γ_l as such a simple function of l_e. Depending on how much of the topographic load consists of mantle material, $\Delta\rho$ may be between $\rho_c - \rho_a$ and $\rho_m - \rho_a$ whereby ρ_m is the uppermost mantle density. Here we adjust l_e, or, in the case of Mars, the lithosphere elastic thickness t_{el}, on which Γ_l depends and which is not the same as t_l, instead of t_c and $\Delta\rho$ instead of ρ_c to optimize the fit. Γ_l also depends on Young's modulus E, Poisson's ratio ν, ρ_m and ρ_c. We adopt $E = 6.5 \cdot 10^{10}$ Pa and $\nu = 0.25$ from Turcotte et al. (1981), and use $\rho_m = 3.338 \cdot 10^3 \mathrm{kg/m}^3$ (see section 3.1) and set $\rho_c = \Delta\rho$.

Figure 1

Fig. 1 shows that for the Earth, Eq. 2 with $\frac{\rho_c}{\rho_0} = 0.49$, corresponding to $\rho_c = 2.70 \cdot 10^3 \mathrm{kg/m}^3$ and $t_c = 45$ km gives a good fit between observed (marked **O**) and modelled crustal (marked **TI**) spectrum above about degree 30. Eq. 3 with $\frac{\Delta\rho}{\rho_0} = 0.25$, corresponding to $\Delta\rho = 1.38 \cdot 10^3 \mathrm{kg/m}^3$ and $l_e = 80$ corresponding to a half-wavelength of 250 km, gives a similarly good fit. For the first case, ρ_c approximately corresponds to independent estimates of (continental) average crustal density. We expect that t_c corresponds to the value around which the largest variations in crustal thickness occur, and that crustal thickness is more variable for thicker crust while the base of the crust (i.e., Moho) is more smooth for thinner crust. This may explain why we obtain t_c somewhat larger than average crustal thickness. We regard this case therefore as more realistic. It is thus implied that globally the gravity signal for degrees $30 < l < 95$ is to a large part due to isostatic crustal thickness variations, confirming that interpretation of gravity in relation to the sublithospheric mantle should be largely restricted to $l \leq 30$ (Steinberger and Holme, 2002). Moreover, only up to $l \approx 13$ is the modelled crustal gravity spectrum substantially less than observed, hence probably only this part of the spectrum is dominated by sublithospheric mantle contributions. Correlation between gravity and topography is high – about 0.7 – above $l \approx 20$, further supporting the interpretation given: A high (in theory, perfect) correlation between gravity and topography should be always expected with shallow gravity causes according to Eqs. 2 or 3, however, gravity anomalies with deeper (mantle) sources may or may not also be highly correlated with the related (dynamic) topography. This issue will be further discussed in the next sections.

Figure 2

The situation for Venus (Fig. 2) is similar to the Earth, in that here Eq. 2 with $\frac{\rho_c - \rho_a}{\rho_0} = 0.55$, corresponding to $\rho_c = 2.95 \cdot 10^3 \mathrm{kg/m}^3$ and $t_c = 60$ km gives a good fit between observed (marked **O**) and modelled crustal (marked **TI-60**) spectrum above about degree 40. For the same reasons as explained for Earth, the value found for t_c may be somewhat larger than the average value of crustal thicknesses, which have e.g. been estimated by Grimm and Hess (1997) and Wieczorek (2007). Eq. 3 with $\frac{\Delta\rho}{\rho_0} = 0.35$, corresponding to $\Delta\rho = 1.83 \cdot 10^3 \mathrm{kg/m}^3$ and $l_e = 76$ corresponding to a half-wavelength of 250 km, gives a similarly good fit. Again, we regard the first case (isostatically compensated crust) as more realistic, because the density contrast required to give a good fit more closely corresponds to expected crustal densities. Below $l \approx 40$, modelled crustal gravity power becomes increasingly smaller compared to observed power with decreasing l. Thus we confirm that a substantial part of gravity power up to $l \approx 40$ may originate in the sublithospheric mantle of Venus (Kiefer and Peterson, 2003).

However, we also note that for degrees 3 to about 50, a very good fit between observed and modeled crustal (marked **TI-900** in Fig. 2) spectrum, with substantially reduced residual gravity (marked **RI-900**) can be achieved with Eq. 2, $t_c = 900$ km and $\rho_c - \rho_a = 1.05 \cdot 10^3 \mathrm{kg/m}^3$. Moreover, the correlation between gravity and topography between degrees 3 and about 30 is even higher (about 0.8) than correlation above about degree 40 (about 0.6). Clearly, this cannot be due to crustal thickness variations, and we will discuss this remarkable result further in the following chapters, in the context of mantle dynamics.

The situation on Mars (Fig. 3) appears somewhat more different: Here a good fit between modeled and observed gravity spectrum can be obtained above $l \approx 10$, either with Eq. 2 with $t_c = 300$ km and $\frac{\rho_c}{\rho_0} = 0.8$, corresponding to $\rho_c = 3.15 \cdot 10^3 \mathrm{kg/m}^3$, or with Eq. 3 with $\frac{\Delta\rho}{\rho_0} = 0.75$ corresponding to $\Delta\rho = 2.95 \cdot 10^3 \mathrm{kg/m}^3$, and the transition between uncompensated and fully compensated topography occurring at a half-wavelength 800 km ($l_e \approx 13$). With the other parameters adopted, this corresponds to $t_{el} = 102$ km. In contrast to Earth and Venus, we regard here the second model (elastic lithosphere) more realistic, because a crustal thickness of 300 km is too large when compared with other estimates which rather indicate a mean crustal thickness around 50 km (Wieczorek and Zuber, 2004; Neumann et al., 2004; Breuer and Spohn, 2003). But of course, for all three planets, the total lithospheric gravity signal is presumably a combination of both effects. Also, with this model, residual gravity is substantially reduced compared to observed gravity between about degrees 14 and 62, and correlation between gravity and topography is high (about 0.8) in this degree range. For degrees 5-15, and especially for degrees 5-10, modelled gravity is higher than observed, and gravity-topography correlation is comparatively low. This presumably indicates that in this degree range topography, including impact basins such as Hellas, is mainly isostatically compensated at shallow depth and therefore not associated with a large gravity signal. We therefore expect a dominating sublithospheric gravity source only up to about degree 5.

Figure 3

3 Radial structure

3.1 Density and pressure profiles

If density ρ is given either as a function of pressure p or radius r, then pressure $p(r)$, total mass $M(r)$ inside radius r and gravity $g(r)$ can be computed by jointly downward-integrating

$$dp = -\rho g(r) dr \tag{4}$$

$$dM = -4\pi\rho r^2 dr \tag{5}$$

$$g(r) = GM(r)/r^2 \tag{6}$$

starting at the surface at r_0 with atmosphere pressure p_a, and mass M_0, which is computed from the more accurately known values GM_0 and G from Mohr and Taylor (2005) (see Table 1).

For the Earth, we adopt the PREM density profile. Based on the considerations in the previous section, we assume a mean crustal thickness $t_c = 60$ km and density $\rho_c = 2.95$ g/cm^3 for Venus. For Mars, we assume $t_c = 50$ km and density again $\rho_c = 2.95$ g/cm^3, consistent with observational constraints (for a review, see Sohl et al., 2005, who also discuss how inferred internal structure depends on assumed values for t_c and ρ_c). Thus Eqs. 4 – 6 are downward-integrated to the base of the crust.

Further downward-integration through mantle and core is done with either of two approaches: The first one uses a given density profile (PREM) to compute pressure as a function of depth in the Earth with Eqs. 4 – 6, and thus infer a pressure-density relation (Fig. 4). Since the CMB in Mars and probably Venus occurs at different pressure than in the Earth, we extrapolate the relations for the lower mantle and outer core (dashed lines). The second approach is to apply a self-consistent model for pressure, temperature and density of the upper mantle (Schmeling et al., 2003; Steinberger and Calderwood, 2006), compiled from available mineral physics data, and jointly downward-integrate with prescribed starting values for pressure, temperature and density. The second approach is mainly used for that part of the Martian mantle in the pressure range of the Earth's "upper mantle" (i.e. above the spinel-perovskite transition at depth ≈ 660 km in the Earth), which is either most or all of the Martian mantle, because PREM features a density decrease with depth below the lithosphere: On the Earth and Venus, this may correspond to lower temperatures (hence higher densities) in the lithosphere. However, for Mars this would imply a density decrease to depths well below the upper thermal boundary layer, and is thus unrealistic.

Figure 4

The downward integration has to match $M(0) = 0$ at the planetary center, but this is normally not the case if we keep the CMB at the same pressure as for the Earth. Hence we modify the depth of the CMB in order to match that constraint. We thus obtain for Venus a core radius 3186 km (0.526 times planetary radius) corresponding to a CMB depth of 2866 km, very similar to the Earth. Resulting profiles of density, pressure and gravity are shown in Figs. 5 . For Mars, the moment of inertia factor 0.3635 (Sohl et al., 2005), which is computed from the density profile, provides an additional constraint, and we hence need to modify either core or mantle density in order to match that constraint as well. If we keep core density unmodified, as inferred from the pressure-density relation in Fig. 4, we can match both constraints (total mass and moment of inertia factor) with the self-consistent upper-mantle computation with starting values for adiabatic temperature 1625 K and density 3362 kg/m^3, and increasing mantle densities below the spinel-perovskite transition by 24 kg/m^3 relative to the Earth (dark lines marked "Mars" in Figs. 4 and 5). In this case, the inferred core radius is 1389.5 km (0.41 times planetary radius), corresponding to a CMB depth of 2000 km, just slightly below the spinell-perovskite ("660") transition at depth 1962 km. However, Sohl et al. (2005) infer a larger core radius from the tidal potential Love number, and also consider core densities likely to be lower. Thus an alternative model with a density starting value 3338 kg/m^3, core density reduced by 1371 kg/m^3 (compared to the extrapolated pressure-density relation for the Earth's core) and core radius 1638.5 km (0.48 times planetary radius), shown as light lines marked "Mars" in Figs. 4 and 5, is also used. We note that these mantle densities are uncertain. For both Mars and Venus, they may be lower than for Earth: Both are convecting in the stagnant-lid regime (e.g., Solomatov and Moresi, 1996; Reese et al., 1998), and as a result, their interiors are likely hotter than Earth. On the other hand, the density of the Martian mantle may be increased due to higher iron content. The second profile doesn't have a spinel-perovskite transition, as the core-mantle boundary occurs at lower pressure. However, the spinel-perovskite transition may also be shallower, if the mantle temperature is hotter, either due to a hotter adiabat or the thermal boundary layer. This is further discussed by van Thienen et al. (2006). Resulting Martian mantle density profiles are very similar to Bertka and Fei (1998). Khan and Conolly (2008) obtain in their preferred model also very similar mantle and core densities, and an even slightly larger core radius of about 1680 km; Zharkov et al. (2009) determine an even larger core radius of 1700-1800 km.

Figure 5

3.2 Mantle temperature and viscosity profiles

Corresponding to the density profiles, we use again two approaches to infer adiabatic temperature profiles. In the first approach we first express temperature as a function of pressure (Fig. 4) for an adiabatic temperature profile for the Earth mantle (Model 2 of Steinberger and Calderwood, 2006). Using the pressure versus depth profiles for the Venus and Mars mantle (Fig. 5) we then express it as a function of depth. This approach is suitable, because the adiabatic temperature profile for the Earth mantle is really also a profile of temperature versus pressure. In the second approach, temperature and pressure are jointly computed as a function of depth, as explained above. Subsequently, thermal boundary layers are added to obtain the full mantle temperature profile (Fig. 6): The temperature profile is modified at the top by adding $(T_a - T_{a,ad}) \cdot [1 - \mathrm{erf}((r_0 - r)/t_l)]$, whereby T_a is surface temperature and $T_{a,ad}$ is the value of the adiabatic profile extended to the surface; we use the lithospheric thicknesses t_l inferred in the previous section as for the thickness of the upper thermal boundary layer. At the bottom, the temperature profile is modified by adding $(T_b - T_{b,ad}) \cdot [1 - \mathrm{erf}((r - r_b/t_b)]$ whereby T_b is temperature at the core-mantle boundary and $T_{b,ad}$ is the value of the adiabatic profile extended to the core-mantle boundary and t_b is the thickness of the thermal boundary layer (TBL) at the base of the mantle and r_b is core radius. For T_b for Venus and t_b for both Venus and Mars we use the same values as Steinberger and Calderwood (2006) for the Earth. The lower T_b for Mars is representative for recent estimates (Sohl and Spohn, 1997; Khan and Conolly, 2008). For the Earth, the somewhat larger values of T_b and t_b, adopted from Steinberger and Holme (2008), correspond to presumed chemically distinct material in some regions near the CMB. Values for T_a, t_l, T_b and t_b are listed in table 1. Assumed surface temperatures have little influence on results, because a high lithosphere viscosity and zero horizontal surface motion are prescribed (see next paragraph).

Figure 6

Computation of viscosity profiles shapes in (Fig. 7) again follows Model 2 of Steinberger and Calderwood, 2006). Absolute viscosity values are unconstrained and also irrelevant for the following chapters. Steinberger and Calderwood (2006) independently varied absolute viscosity values in the lithosphere, upper mantle, transition zone and lower mantle of the Earth to match various observational constraints. The resulting best-fit viscosity profile increases gradually with depth in the upper and lower mantle, but also has a jump of about a factor 10 between upper and lower mantle. Earlier models assumed layers of constant viscosity and hence inferred a larger viscosity jump (e.g., Hager and Richards, 1989). For Mars and Venus, we do not have such constraints;

Figure 7

thus we do not consider different viscosity jumps across the olivine-spinel transition. A slight viscosity decrease from above to below the transition corresponds to a slight temperature increase. But different mineralogy below the transition may cause higher viscosity. On the other hand, viscosity may be reduced due to higher water content. Thus, for Mars and Venus even more than for Earth, the viscosity contrast across the olivine-spinel transition is poorly known. For Venus, we do, however, consider two different cases for lower vs. upper mantle viscosity, i.e. viscosity jumps across the spinel-perovskite transition. In the first case, there is only a slight increase of viscosity across the transition, corresponding to the temperature decrease. In the second case, viscosity below the transition is increased by a factor 4 relative to the first case, such that the resulting viscosity profile approximately matches best-fit profiles inferred for Earth by Steinberger and Calderwood (2006). For Mars, we also tested models with a viscosity jump at the olivine-spinel transition or at a shallower depth, but found that adding a substantial jumpwise viscosity increase generally deteriorates the fit between model and observations (results not shown). On the other hand, Roberts and Zhong (2006) showed that to produce long-wavelength structures such as Tharsis or crustal dichotomy for Mars with stagnent-lid convection, a weak olivine layer or asthenosphere is required. Keller and Tackley (2009) propose a mid-mantle viscosity jump to obtain a "one-ridge convection" that is able to produce crustal dichotomy. Since both Venus and Mars appear both characterized by a rigid lithosphere, we set viscosity in the upper 100 km to a high value 10^{23} Pas and prescribe a rigid upper boundary condition for horizontal motion. For the following computations, layers of constant viscosity are a technical requirement. We therefore divide the mantle below 100 km up in layers of about 100 km thickness with constant viscosity, however in such a way that the viscosity jumps in Fig. 7 are maintained.

4 Predicted gravity and topography spectra and comparision with observations

Gravity potential expansion coefficients can be computed for density expansion coefficients $\delta {\rho_c}_l^m(r)$:

$$C_l^m = \frac{3}{(2l+1)\rho_0 r_0} \int_{r_b}^{r_0} K_l(r) \delta {\rho_c}_l^m(r) dr \tag{7}$$

and likewise for S_l^m and and $\delta {\rho_s}_l^m(r)$, with integration from CMB radius r_b to surface radius r_0. $K_l(r)$ are the so-called geoid kernels which specify how much gravity anomaly at the Earth surface a density anomaly at a given depth causes. They can be computed for a viscous mantle model with radial viscosity variations and contain contributions of both the initial density variations (that drive flow) and the (surface and CMB) boundary displacements caused by the flow. In an analogous way, dynamic topography kernels $K_l^t(r)$ specify how much dynamic topography a density anomaly at a given depth causes. They are normalized such that they approach unity towards a stress-free surface (corresponding to isostasy).

Fig. 8 shows both geoid kernels and topography kernels for models of Earth, Venus and Mars, computed with a self-consistent gravity model and for a compressible mantle. The viscosity model for Earth is derived in the same way as Model C of Steinberger and Holme (2008), but with the additional requirement that the lowest viscosity occurs in the upper mantle, not the transition zone. As in that paper, we also assume here for Earth a free upper surface, but with a high-viscosity $2.2 \cdot 10^{22}$ Pas lithosphere, consistent with assuming radial viscosity variations only, and appropriate to obtain a good fit between modeled and observed geoid. The viscosity model and kernels shown for Venus is without a viscosity increase across the spinel-perovskite transition. In contrast, we assume zero horizontal motion, and zero normal stress at the surface, and 10^{23} Pas lithosphere viscosity for Venus. This corresponds to a rigid lithosphere, but with sufficiently small elastic thickness such that its vertical displacement corresponds to the forces acting from below. Anderson and Smrekar (2006) also find that for a large part of the Venusian lithosphere, elastic thickness is sufficiently small such that one cannot distinguish from isostasy. Given that we expect the mantle signal to be important for up to degree 40 for Venus, l_e needs to be larger than that for the isostatic approximation to be appropriate. With the values for E and ν from Table 1, $l_e > 40$ corresponds to $t_{el} < 70$ km, which is confirmed by a number of studies (Simons et al., 1997; Phillips et al., 1997; Barnett et al., 2002). **Figure 8**

For Mars, we also assume zero horizontal motion, but here the elastic thickness presumably cannot be neglected. In analogy to Eq. 3 and the discussion in section 2, we assume here that the lithosphere deflection is only a fraction Γ_l' of that corresponding to a surface free of vertical stresses. Zhong (2002) has shown that the Turcotte et al. (1981) thin shell formulation is also appropriate for such internal loads. However, we note that Turcotte et al. (1981) implicitly assume (as stated in their paper) that the region between zero level and downward displacement w of the lithosphere is filled with crust of density ρ_c. As this assumption is probably not appropriate for internal loads, we modify here their equations (6) and (7) by replacing $\rho_m - \rho_c$ with ρ_m, thus the fraction Γ_l' for lithosphere deflection through internal loads differs from Γ_l. Consequently, topography kernels reach a maximum less than 1 near the surface, and geoid kernels do not approach zero in the limit of zero depth. We show here the case with larger core radius.

For all three planets, a stress-free core-mantle boundary is assumed. In the case of Mars, it is not certain whether the core is liquid or solid. However, depending on core viscosity, even in the case of a solid core, a stress-free core-mantle boundary may be more appropriate and, in any case, core and mantle are largely decoupled by a low viscosity in the lowermost mantle; kernels stay therefore similar even if zero horizontal velocity at the core-mantle boundary is imposed instead. The thermal effect of phase boundaries on dynamic topography and geoid is included: For a given temperature anomaly, the deflection of a phase boundary with Clapeyron slope γ and density contrast $\Delta\rho_{pb}$ has the same effect as the density anomaly due to thermal expansivity α in a layer of thickness $\Delta z = \frac{\gamma \Delta\rho_{pb}}{\rho^2 \alpha g}$. That is, a phase boundary with positive Clapeyron slope essentially doubles the effect over a thickness Δz, whereas a phase boundary with negative Clapeyron slope compensates a thickness $|\Delta z|$. We use $\gamma\Delta\rho_{pb} = 435\mathrm{MPa/K} \cdot \mathrm{kg/m}^3$ for the olivine-spinel transition ($\approx$ 400 km deep in the Earth) and $300\mathrm{MPa/K} \cdot \mathrm{kg/m}^3$ for the combined effect of the spinel-perovskite and majorite-perovskite transition ($\approx$ 660 km deep in the Earth) – see Steinberger (2007) for a discussion of these values and original references. We use $\alpha = 2.378 \cdot 10^{-5}/\mathrm{K}$ for the olivine-spinel and $2.081 \cdot 10^{-5}/\mathrm{K}$ for the spinel/majorite-perovskite transition, based on Steinberger and Calderwood (2006) and references therein. In Fig. 8 the phase boundaries appear as narrow spikes. The Mars model shown here only includes the olivine-spinel transition.

Based on these kernels, we now compute expected geoid-to-topography ratios and correlations as a function of spherical harmonic degree and compare with observed values. Whether or not a good match is obtained tells us whether it is likely that both geoid and topography are caused dynamically in the mantle, and should both be considered in our further analysis.

At each depth r, $\delta{\rho_c}_l^m$ and $\delta{\rho_s}_l^m$ are assumed to be taken from a normal distribution with zero mean and standard deviation $\sigma_l(r)$. If furthermore density anomalies at radii r and r' have an expected correlation of $c(r, r')$, then the expected gravity power at degree l is

$$E[\langle P_l \rangle] = \frac{l+1}{2l+1} \left(\frac{3}{\rho_0 r_0} \right)^2 \int_{r_b}^{r_0} \int_{r_b}^{r_0} K_l(r) \sigma_l(r) K_l(r') \sigma_l(r') c(r, r') dr dr' \tag{8}$$

$c(r, r')$ should be 1 for $r = r'$ and become smaller for larger $|r - r'|$. We shall here use $c(r, r') = \exp(-(r-r')^2/d_l^2)$, with a radial correlation length $d_l = d_0/l$, i.e. proportional to the wavelength in horizontal direction. This approximately corresponds to the simpler procedure used by Steinberger and Holme (2002) of summing over N radial layers, whereby an additional factor $1/l$ was introduced in most cases in order to compensate for using layers of constant thickness rather than inversely proportional to l. Like for Steinberger and Holme (2002), our computations are not for simply one random density model, but for the expected average of a large number of random models. This average is, however, computed analytically, not by actually averaging over a large number of models. Actual tomography models indicate a less strong dependence of d_l on l, and also some dependence on r (T. Becker, pers. comm.). However, there is considerable model dependence due to radial smearing. Because of these uncertainties, we regard assuming a $1/l$ dependence – which essentially means that the aspect ratio of density anomalies is independent of length scale – as appropriate. It also turns out that this assumption tends to give a better fit between modeled and observed gravity power than assuming a weaker dependence on l. We will use here $d_0 = r_0/4$ for all three planets. As long as d_0/l is substantially smaller than the thickness of the mantle – as is the case here – the l-dependence of expected gravity power does not strongly depend on d_0. Once d_0/l becomes similar to or larger than mantle thickness, expected gravity power decreases less strongly with l and we find that the fit to data tends to overall somewhat deteriorate.

For expected dynamic topography power $E[\langle P_l^t \rangle]$, the factor $\frac{1}{2l+1}\left(\frac{3}{\rho_0}\right)^2$ is replaced by $(2l+1)\frac{1}{(\rho_m-\rho_a)^2}$ whereby $\rho_m - \rho_a$ is the appropriate surface density contrast – difference between uppermost mantle density and surface atmospheric density (see Table 1). In the case of an elastic lithosphere (as assumed for Mars), the factor Γ_l' is already included in the topography kernels $K_l^t(r)$.

For simplicity, we shall assume further that the standard deviation of density variations can be expressed as product of an l-dependent and an r-dependent factor i.e. $\sigma_l(r) = \sigma_{1,l} \cdot \sigma_2(r)$, and define for brevity $K_l(r) \cdot \sigma_2(r) =: G_l(r)$ and $K_l^t(r) \cdot \sigma_2(r) =: T_l(r)$. We will furthermore assume that the standard deviation of relative density variations is independent of radius, i.e. we will use $\sigma_2(r) = \rho(r)$

The expected geoid-to-topography ratio is then independent of $\sigma_{1,l}$

$$\sqrt{\frac{E[\langle P_l \rangle]}{E[\langle P_l^t \rangle]}} = \frac{3(\rho_m - \rho_a)}{\rho_0(2l+1)} \sqrt{\frac{\int_{r_b}^{r_0}\int_{r_b}^{r_0} G_l(r) G_l(r') c(r,r') dr dr'}{\int_{r_b}^{r_0}\int_{r_b}^{r_0} T_l(r) T_l(r') c(r,r') dr dr'}} \tag{9}$$

With $\int_{r_b}^{r_0} G_l(r)dr/(r_0 - r_b) =: \bar{G}_l$ and $\int_{r_b}^{r_0} T_l(r)dr/(r_0 - r_b) =: \bar{T}_l$ the expected correlation between geoid and topography is

$$E[\left\langle C_l^{tg} \right\rangle] = \frac{\int\limits_{r_b}^{r_0}\int\limits_{r_b}^{r_0} \left(G_l(r) - \bar{G}_l\right)\left(T_l(r') - \bar{T}_l\right) c(r,r') dr dr'}{\sqrt{\int\limits_{r_b}^{r_0}\int\limits_{r_b}^{r_0} \left(G_l(r) - \bar{G}_l\right)\left(G_l(r') - \bar{G}_l\right) c(r,r') dr dr' \int\limits_{r_b}^{r_0}\int\limits_{r_b}^{r_0} \left(T_l(r) - \bar{T}_l\right)\left(T_l(r') - \bar{T}_l\right) c(r,r') dr dr'}} \tag{10}$$

Figure 9

Fig. 9 compares the expected geoid power, geoid-topography ratio and correlation for our models with respective data. We now first discuss the latter two, because modeling those requires no further assumption about magnitude and spectral dependence of density anomalies. To assess how significant the difference between model and data is, we also estimate the expected standard deviation of geoid-topography ratio and correlation: With a radial correlation length $d_l = d_0/l$ there are approximately $l \cdot (r_0 - r_b)/d_0)$ independent radial layers, and we therefore take $1/\sqrt{l \cdot (r_0 - r_b)/d_0)}$ as a crude estimate for the expected relative standard deviation of both the geoid-topography ratio and the departure from perfect correlation or anticorrelation. Thus, our crude estimate for the expected standard deviation of the correlation coefficient is $(1 - E[\left\langle C_l^{tg} \right\rangle]) \cdot (1 + E[\left\langle C_l^{tg} \right\rangle])/ \cdot \sqrt{l \cdot (r_0 - r_b)/d_0)}$.

For Earth, the geoid-topography ratio predicted from our mantle dynamic model is typically several times higher than observed except for degrees 2 and 3. This comes as no surprise, as Earth topography is known to be largely caused by crustal thickness variations. To utilize topography information for drawing inferences on mantle dynamics requires extracting the "dynamic" topography signal from the observed topography, which is a notoriously difficult problem. Here we shall not further consider Earth topography.

For Venus, on the other hand, predicted and observed geoid-topography ratio match much better, in particular for the model with no additional viscosity increase across the spinel-perovskite phase transition (shown as solid line) which indicates that here topography could be to a large part "dynamic" i.e. supported by mantle density anomalies and flow. The match becomes almost perfect if the lithospheric contribution as inferred from observations (grey lines) is also considered, except for a somewhat too high predicted ratio for degrees 2-4. This interpretation is also supported by the high geoid-topography correlation, both observed and modeled (solid line). The fact that observed correlation is somewhat smaller than modeled, and generally gradually decreases with increasing l can be due to additional, but generally smaller lithospheric contributions. The one major discrepancy occurs for degree 2, with rather low observed geoid-topography correlation. This is related to the very low amplitude of the degree 2 geoid, which will be further addressed below.

For Mars, modeled geoid-topography ratio matches with observations up to degree 4, thus indicating that up to degree 4 dynamic topography should be of similar amplitude as total topography. For degrees 4 and lower, we find that a substantial part of topography could also be dynamically supported. The grey continuous line shows that for a combination of modeled lithosphere and mantle contributions, the geoid-topography ratio can be fitted better for the degree range shown, but is generally predicted too large, especially at degrees 5-10, indicating again that probably a large part of topography in this degree range is compensated at shallower levels. On the other hand, modeled and observed geoid-topography correlations do not match well, except for degree two, which shows that topography other than dynamically supported is probably also of similar amplitude as total topography for all degrees, with the possible exception of degree two.

As for Earth, the difficulty to use "raw" topography information to draw inferences on the internal dynamics can be attributed to large crustal thickness variations, and we shall not further address this issue here. Our result, that a large part of Martian topography up to degree 4 could be dynamically supported, should, however motivate future work to address this issue.

While Earth density anomalies can be estimated based on tomography, no such information is available for other planets. It is, however, possible to apply a spectral dependence of density anomalies inferred from tomography (on Earth) to predict expected gravity (and topography) spectra on Mars and Venus: We assume

$$\sigma_{1,l} = \sigma_0/\sqrt{(l+1)(2l+1)} \tag{11}$$

(based on Becker and Boschi, 2002, Figure 2): Then the expected power at degree l is

$$E[\langle P_l \rangle] = \left(\frac{3\sigma_0}{(2l+1)\rho_0 r_0}\right)^2 \int_{r_b}^{r_0}\int_{r_b}^{r_0} G_l(r)\rho(r)G_l(r')c(r,r')drdr' \tag{12}$$

As there are $2l+1$ coefficients of degree l we take $1/\sqrt{2l+1}$ as a crude estimate for the expected relative standard deviation.

In the top left panel of Fig. 9, we compare the thus predicted gravity power spectrum for two Earth models with observations. The viscosity model, and other model assumptions for the solid line are very similar to the "best-fit" case discussed by Steinberger and Holme (2002) and thus the result and good fit remains similar. We use $\sigma_0 = 0.08\%$ to get a good fit, and with this value, Eq. 11 gives relative density variations in overall agreement with what is inferred from tomography models (Becker and Boschi, 2002, Fig. 2) taking into account the different normalization of spherical harmonics used (see e.g. Wieczorek, 2007), and the conversion factor from relative seismic velocity to relative density variations expected for temperature variations (about 0.25).

The dashed line is included here, because for the corresponding viscosity model yields in fact a better fit between predicted and observed geoid. However, the spectrum is less well fit. We thus illustrate that, even for Earth, the geoid spectrum is a valuable additional constraint on mantle flow models, and, in particular, yields support to a model with lowest viscosity just below the lithosphere, rather than in the transition zone.

In the top center panel, the same comparision is done for Venus: here we get a good match between predicted and observed gravity power from degree 5 upward with $\sigma_0 = 0.12\%$, if we consider both mantle and lithosphere contribution, with the lithosphere contribution (dotted line) becoming dominant above $\approx$ degree 31. Observed gravity power for degrees 2-4 is much lower than predicted; the mismatch is especially large for degree 2.

For Mars (top right panel) the combination of mantle contribution (with $\sigma_0 = 0.22\%$) and lithosphere contribution allows a good fit for all degrees shown. Here the lithosphere contribution becomes already dominant from degree 6 upward, such that we can draw inferences on mantle density structure only up to about degree 5.

We now use these results to tentatively infer mantle density structures for Mars and Venus. Obviously, we can only estimate a radially averaged lateral structure. The result for Mars (Fig. 10) is thus computed from the observed degree 2-5 geoid and the kernels in Fig. 8 with Eq. 7 **Figure 10** assuming the density anomaly is not varying with radius. For Venus, degrees 2-40 are used. For Venus, we correct gravity for the topography effect (as in Fig. 2, line marked **RI-60**), whereas we do not correct for Mars. As discussed below the topography correction for Mars is proably inappropriate in the degree range 2-5.

On Venus, geoid power is very low for degrees 2-4, but from degree 5 onward, we find geoid kernels close to zero in its lower mantle. Hence the geoid on Venus gives little indication regarding its lower mantle density structure. The average (Fig. 10) essentially represents the upper 800 km. However, our results indicate that density anomalies at degrees 2-4 (especially degree 2) in the lower mantle of Venus are much smaller than for Earth - the geoid kernels imply that larger anomalies would also cause a larger geoid signal at these low degrees. In contrast, the degree 2-5 density structure inferrered for Mars may well primarily reside in its lower mantle.

5 Discussion, with emphasis on the relation between density anomalies in the lower mantle and volcanism

The motivation for this study has been to analyse which part of the gravity and topography spectra of Earth, Mars and Venus may be primarily due to density anomalies and viscous flow beneath their lithospheres. From the corresponding parts of the gravity field, we inferred mantle density anomalies, in order to relate them to volcanism. Compared to previous work addressing similar issues, we regard the main new features of our work (1) using radial mantle viscosity models consistent with mineral physics and (2) using a spectral dependence of mantle density anomalies derived from seismic tomography on Earth. This spectral dependence is an empirical observation, and therefore cannot necessarily be transferred to other planets. In particular, we find that with this spectral dependence our models for Venus always vastly overpredict the geoid for spherical harmonic degrees 2-4. This misfit remains puzzling, and we cannot avoid the conclusion that for Venus, density anomalies in this degree range are much less, compared to higher degrees, than inferred from tomography (Eq. 11) for Earth: If there were similarly large large-scale density anomalies, they should also cause much larger gravity anomalies. Moreover, the lower-than-predicted geoid-topography ratio indicates that the density anomalies causing geoid anomalies and topography are mainly located at "shallow" depth where geoid kernels are small compared to topography kernels.

Earth structure appears to be dominated by low degrees, in particular degree two, and hence a geotectonic bipolarity (Pavoni, 1981) is found. In particular, two LLSVPs are the dominant feature of the lowermost mantle, and plumes appear to be rising from their edges. For Venus, our results give no evidence for such large structures – in particular not in its lower mantle, and therefore there is no evidence for a relation of volcanism and lowermost mantle structure.

This apparent absence of large-scale structures in Venus may be related to its lack of plate tectonics, at least during the past few hundred Myr: Earth's LLSVPs are primarily in regions where no subduction has occurred during the past 300 Myr, so there is reason to believe that the existence and location of LLSVPs is in some way related to plate tectonics – although the exact cause-and-effect relation remains enigmatic. On the other hand, Roberts and Zhong [2006] showed that long-wavelength structures can be generated for stagnant-lid convection with no plate tectonics, but with a different viscosity structure than assumed here.

Between degrees 5 and ≈ 40, however, our model explains well both the geoid power spectrum and geoid-topography ratio for Venus. Our results indicate a dominant mantle contribution to Venusian geoid and topography up to degree 40. This result basically confirms the results of Pauer et al. (2006), who did computations for a larger number of viscosity models. They find that viscosity profiles with an increase up to a factor 10-80 across the mantle allow a good fit to the data. In accordance, we find a better fit for our model with no additional viscosity increase across the spinel-perovskite transition [total viscosity increase through the mantle by about a factor 100], compared to the model with additional increase [total increase $\approx$ factor 400]. Geoid (and topography) kernels for our preferred model of Venus in this degree range are mostly sensitive to upper mantle structure, with geoid (and topography) highs corresponding to low density. We can therefore tentatively estimate upper mantle density structure of Venus, with low density underlying geoid and topography highs. The resulting density map can be interpreted as indication for the presence of plumes, at least in the upper mantle, beneath geoid and topography highs.

There is also a clear relation between regions which we predict to be underlain by low-density upper mantle and the distribution of rift zones and lobate plains, which are the youngest volcanic materials on the surface of Venus: Rift zones (shown in black in Fig. 10, middle panel) are radiating away from the two regions where our model predicts the strongest negative density anomalies in the upper mantle, below -0.5 % at about 282° E, 25° N (Beta Regio) and below -0.3 % at 200° E, 0° N (near Atla Regio; mostly covered and poorly visible). With upper mantle thermal expansivity of about $3 \cdot 10^{-5}$/K (e.g., Fig. 1 in Schmeling et al., 2003; see also the compilation in Steinberger and Calderwood, 2006, for further references), -0.3 – -0.5 % density anomaly corresponds to a temperature anomaly in the order of 100–170 K. Due to lack of resolution, this may be an underestimate of actual maximum temperature anomalies; it is lower than typical estimates for mantle plumes on Earth ($\approx$ 200–300 K). The importance of hot, low density, upwelling mantle at these and other volcanic rises on Venus has been previously recognized (Kiefer and Hager, 1991; Herrick and Phillips, 1992; Grimm and Phillips, 1992; Solomatov and Moresi, 1996; Smrekar et al., 1997; Kiefer and Peterson 2003). Kiefer and Hager (1991) also point out that, for models to match the observed geoid and topography of these features, Venus must lack an Earth-like low-viscosity zone in its upper mantle. Similarly, our preferred model for Venus has less viscosity increase with depth than the preferred Earth model. More generally, lobate plains (Fig. 10, middle panel) are mostly where our model indicates low-density upper mantle and less frequent in regions with high-density upper mantle.

For Mars, on the other hand, we can match the predicted and observed geoid spectrum reasonably well with an elastic lithosphere with $l_e \approx 13$ for the transition between isostatic compensation of loads (for small l) and no compensation (for large l). With the parameters adopted, this corresponds to an elastic lithosphere thickness of 102 km. This is similar to, but in the upper range of some other estimates (McGovern et al., 2002 and correction in 2004; Belleguic et al., 2005; see also the review by Wieczorek, 2007). However, Phillips et al. (2008) find a much larger elastic thickness from the deflection of the lithosphere due to ice load. We therefore regard the values of t_{el} and l_e inferred here as compatible within uncertainties. The geoid power due to topography is overpredicted mainly in the degree range 5-10, and the geoid-topography ratio is also over-predicted. This discrepancy can be reduced by increasing l_e, corresponding to reducing elastic thickness, as then topography in the degree range 5-10 becomes more nearly isostatically compensated, thus causing less geoid power. But this makes the fit between predicted and observed gravity power worse. An explanation for the over-prediction of geoid power due to topography is therefore that a large part of topography in the degree range 5-10 is isostatically compensated at shallow depth, e.g. due to crustal thickness and density variations, and therefore causes smaller gravity anomalies.

Obviously, our results depend on a number of assumptions, such as thickness of thermal boundary layers, temperature drops in the bottom boundary layer, mantle density etc., and it may well be that another combination of "reasonable" assumptions leads to an even better fit between model and data. A systematic exploration of parameter space is, however, beyond the scope of this paper. Our purpose is more limited in that we show that – with parameters that are mainly adopted from elsewhere – our model can give a rather good fit to large parts of the gravity spectra for Earth, Mars and Venus and to the geoid-topography ratio of Venus, and we expect that this finding increases the plausibility of our model. In fact, there are essentially three to four adjustable parameters in our models of gravity power (and only one to two of those related to the sublithospheric mantle): The lithosphere contribution is chosen such that the combination gives a good fit to parts of the gravity spectrum presumed to be dominated by the lithosphere: $40 < l \leq 95$ for Venus, $30 < l \leq 95$ for Earth, $6 \leq l \leq 22$ for Mars. Essentially the dotted lines in the top panels of Fig. 9 can be shifted up and down, and its slope changed. This lithosphere contribution can be explained as caused by topography that is isostatically compensated at the base of the crust, or loads an elastic lithosphere from above, with reasonable values for crustal thickness and densities, or l_e (see Eq. 3). σ_0 on the other hand allows to shift the part of the curves dominated by the mantle (or all of the black curves) up and down. For the Earth, $\sigma_0 = 0.08\%$ is consistent with density anomalies inferred from tomography. The value σ_0 for Venus is larger by a factor 1.5. A larger value for Venus is surprising, because convection in the stagnant lid regime (Venus case) typically has smaller temperature variations in the mantle than convection in the plate tectonics regime (Earth case) (e.g., Gurnis, 1989). However, this larger value is inferred from degrees 5 and above, and may be the counterpart of much lower power for degrees 2–4. For Mars, the inferred value σ_0 is larger by a factor 2.75 than for Earth, and this may correspond to higher thermal expansivities in the Martian mantle, which is within the pressure range of the Earth's upper mantle. In the case of an elastic lithosphere we also adjust the value l_e corresponding to the wavelength where the lithosphere deflection is half the isostatic value.

With regard to large-scale density structure, the Earth appears more similar to Mars than to Venus, as the Martian mantle also appears dominated by low-degree structure, in particular degree two. For degrees 6 and above, gravity sources from within the thick Martian lithosphere appear to be dominant, but some inferences on mantle structure (beneath the lithosphere) up to degree 5, and its relation to surface volcanism can probably be drawn. The predicted mantle density structure shown in Fig. 10, when converted to temperatures, is similar to Kiefer et al. (1996), but we also consider the effect of the elastic lithosphere and limit our prediction to degrees 2-5 where the mantle contribution to the geoid appears to be dominant according to our spectral analysis.

The Martian mantle density structure appears to be characterized by two large antipodal low-density anomalies and upwellings approximately centered on the equator. Maximum inferred density anomalies (below Tharsis) exceed 0.6 %, corresponding to ≈ 200 K temperature anomaly. However, this density structure was derived for a chemically homogeneous mantle. Like suspected for the Earth, there could be chemically distinct and heavier LLSVPs at the base of large-scale upwellings. The presence of these heavier piles can give a very similar geoid signal as the upward deflection of the CMB that would result without them (Steinberger and Holme, 2008), and, as for Earth, their existence could be related to plate tectonics, which may have have occurred at an early stage of the Martian tectonic evolution. With our model we cannot distinguish from what depth the large-scale geoid highs on Mars originate, and whether or not there are chemically distinct LLSVPs at the base of the Martian mantle. The prominent volcano Olympus Mons as well as the Elysium volcanoes occur at the margin of the inferred density lows but other volcanoes (Tharsis) sit right on top of the presumed density lows. Overall, volcanics (shown in Fig. 10, bottom panel) tend to mostly occur in regions with inferred low mantle densities, but there is no obvious relation with the margins of such regions. However, most of the volcanic activity had ceased early in the Martian history and continues only in the Tharsis province until recently (Werner, 2008). On Earth, though, reconstructed LIP eruption locations (shown in Fig. 10, top panel) tend to overlay LLSVP margins, but are absent above LLSVP centers.

Our results indicate that, as on Earth, also on Mars the distribution of volcanism appears to be related to large-scale mantle structure, and both distribution of volcanism and large-scale mantle structure appear to be stable for long times. On Venus, on the other hand, our method is limited to mantle structure above about 800 km depth. Whereas on Earth we attribute long-term stability to the existence of chemically distinct LLSVPs in the lowermost mantle, our results remain inconclusive on the causes of long-term stability of the Martian mantle.

Acknowledgement

This work was partly done during visits of B.S and T.H.T to Freie Universität Berlin, funded by the German Academic Exchange Service (DAAD) and The Research Council of Norway. We thank Mikhail Ivanov for providing geologic features on Venus in digital form, and Richard Holme, members of the Planetary Physics group at DLR, Alexander Basilevsky, Boris Ivanov, Thorsten Becker and Thomas Ruedas for ideas, suggestions and discussions, and Shijie Zhong and an anonymous reviewer for their comments which substantially improved the manuscript.

REFERENCES CITED

Anderson, D.L., 2000. The thermal state of the upper mantle: No role for mantle plumes. Geophys. Res. Lett. 27, 3623–3626.

Anderson, F.S., Smrekar S.E., 2006. Global mapping of crustal and lithospheric thickness on Venus. J. Geophys. Res. 111, E08006, doi:10.1029/2004JE002395.

Barnett, D.N., Nimmo, F., McKenzie, D., 2002. Flexure of Venusian lithosphere measured from residual topography and gravity. J. Geophys. Res. 107, 5007, doi:10.1029/2000JE001398.

Becker, T.W., Boschi, L., 2002. A comparison of tomographic and geodynamic mantle models. Geochem. Geophys. Geosyst. 3, 2001GC000168.

Belleguic, V., Lognonné, P., Wieczorek, M., 2005. Constraints on the Martian lithosphere from gravity and topography data, J. Geophys. Res. 110, E11005, doi:10.1029/2005JE002437.

Bertka, C.M., Fei, Y., 1998. Density profile of an SNC model Martian interior and the moment-of-inertia factor of Mars. Earth Planet. Sci. Lett. 157, 79–88.

Breuer, D., Spohn, T., 2003. Early plate tectonics versus single-plate tectonics on Mars: Evidence from magnetic field history and crust evolution, J. Geophys. Res. 108, 5072, doi:10.1029/2002JE001999.

Clairaut, M., 1743. Théorie de la figure de la terre, tirée des principes de l'hydrostatique. Ches David fils, Paris.

Daradich, A., Mitrovica, J.X., Matsuyama, I., Taylor Perron, J., Manga, M., Richards, M.A., 2008. Equilibrium rotational stability and figure of Mars. Icarus, 194, 463–475.

Davies, G.F., 2005. A case for mantle plumes. Chin. Sci. Bull. 50, 1541–1554.

Dziewonski, A.M., Anderson, D.L. 1981. Preliminary Reference Earth Model. Phys. Earth Planet. Inter. 25, 297–356.

Eldholm, O., Coffin, M.F., 2000. Large Igneous Provinces and Plate Tectonics. In: Richards M.A., Gordon, R.G., van der Hilst, R.D. (Eds.), The History and Dynamics of Global Plate Motions, American Geophysical Union, Washington, pp. 309–326.

Fukao, Y., Widiyantoro, S., Obayashi, M., 2001. Stagnant slabs in the upper and lower mantle transition region. Rev. Geophys. 39, 291–323.

Greeley, R. and Guest, J.E., 1987. Geological Map of the Eastern Equatorial Region of Mars (1:15,000,000). USGS Misc. Inv. Series map I-1802-A.

Grimm, R.E., Hess, P.C., 1997. The Crust of Venus. In: Bougher, S.W., Hunten, D.M., Phillips, R.J. (Eds.), Venus II, Univ. of Arizona Press, Tucson, pp. 1205–1244.

Grimm, R.E., Phillips R.J., 1992. Anatomy of a Venusian Hot Spot: Geology, Gravity, and Mantle Dynamics of Eistla Regio, J. Geophys. Res., 97, 16,035–16,054.

Gurnis, M., 1989. A reassessment of the heat transport by variable viscosity convection with plates and lids. Geophys. Res. Lett. 16, 179–182.

Hager, B.H., 1984. Subducted slabs and the geoid: constraints on mantle rheology and flow. J. Geophys. Res. 89, 6003–6015.

Hager, B.H., Richards, M.A., 1989. Long-wavelength variations in Earth's geoid: physical models and dynamical implications. Philos. Trans. R. Soc. London, Ser. A 328, 309–327.

Heeremans, M., Faleide, J.I., Larsen, B.T., 2004. Late Carboniferous Permian of NW Europe: an introduction to a new regional map. In: Wilson, M., Neumann, E.-R., Davies, G.R., Timmerman, M.J., Heeremans, M., Larsen, B.T. (Eds.), Permo-Carboniferous Magmatism and Rifting in Europe, Geological Society London Special Publication 223, pp. 75–88.

Herrick, R.R., Phillips, R.J., 1992. Geological Correlations With the Interior Density Structure of Venus. J. Geophys. Res. 97, 16,017–16,034.

Hipkin, R.G., 2001. The statistics of pink noise on a sphere: applications to mantle density anomalies. Geophys. J. Int. 144, 259–270.

Ivanov, M.A., 2008. Global geological map of Venus: Preliminary results. Lunar and Planetary Science XXXIX (2008)

Keller, T., Tackley, P.J., 2009. Towards self-consistent modeling of the martian dichotomy: The inuence of one-ridge convection on crustal thickness distribution. Icarus 202, 429–443.

Khan, A., Connolly, J.A.D., 2008. Constraining the composition and thermal state of Mars from inversion of geophysical data. J. Geophys. Res. 113, E07003, doi:10.1029/2007JE002996.

Kiefer, W, Bills, B.G., Nerem, R.S., 1996. An inversion of gravity and topography for mantle and crustal structure on Mars. J. Geophys. Res. 101, 9239–9252.

Kiefer, W. S., Peterson, K., 2003. Mantle and crustal structure in Phoebe Regio and Devana Chasma, Venus. Geophys. Res. Lett. 30, 1005, doi:10.1029/2002GL015762.

Kiefer, W.S., Hager, B.H., 1991. A Mantle Plume Model for the Equatorial Highlands of Venus, J. Geophys. Res. 96, 20,94720,966.

Konopliv, A.S., Yoder, C.F., Standish, E.M., Yuan, D.-N., Sjogren, W.L., 2006. A global solution for the Mars static and seasonal gravity, Mars orientation, Phobos and Deimos masses, and Mars ephemeris. Icarus 182, 23–50.

Konopliv, A., 2006. online at
http://pds-geosciences.wustl.edu/missions/magellan/shadr_topo_grav/index.htm

Lowry, A.R., Zhong, S., 2003. Surface versus internal loading of the Tharsis rise, Mars. J. Geophys. Res. 108, 5099, doi:10.1029/2003JE002111.

Mayer-Gürr, T., Eicker, A., Ilk, K.-H., 2007. ITG-Grace03 Gravity Field Model. online at http://www.geod.uni-bonn.de/itg-grace03.html

McGovern, P.J., Solomon, S.C., Smith, D.E., Zuber, M.T., Simons, M., Wieczorek, M.A., Phillips, R.J., Neumann, G.A., Aharonson, O., Head, J.W., 2002. Localized gravity/topography admittance and correlation spectra on Mars: Implications for regional and global evolution, J. Geophys. Res. 107, 5136, doi:10.1029/2002JE001854.

McGovern, P.J., Solomon, S.C., Smith, D.E., Zuber, M.T., Simons, M., Wieczorek, M.A., Phillips, R.J., Neumann, G.A., Aharonson, O., Head, J.W., 2002. Correction to “Localized gravity/topography admittance and correlation spectra on Mars: Implications for regional and global evolution”, J.

Geophys. Res. 109, E07007, doi:10.1029/2004JE002286.

McKenzie, D., Fairhead D., 1997. Estimates of the effective elastic thickness of the continental lithosphere from Bouguer and free air gravity anomalies, J. Geophys. Res. 102, 27,523–27,552.

Mohr, P.J., Taylor, B.N., 2005. CODATA recommended values of the fundamental physical constants: 2002. Rev. Mod. Phys. 77, 1–107.

Nakiboglu, S.M., 1982. Hydrostatic theory of the Earth and its mechanical implications, Phys. Earth Planet. Int. 28, 302–311.

Neumann, G.A., Zuber, M.T., Wieczorek, M.A., McGovern, P.J., Lemoine, F.G., Smith D.E. (2004), Crustal structure of Mars from gravity and topography, J. Geophys. Res. 109, E08002, doi:10.1029/2004JE002262.

Pauer, M., Fleming K., Čadek, O., 2006. Modeling the dynamic component of the geoid and topography of Venus. J. Geophys. Res. 111, E11012, doi:10.1029/2005JE002511.

Pavoni, N., 1981. A global geotectonic reference system inferred from Cenozoic tectonics. Geol. Rdsch. 70, 189–206.

Phillips, R.J., Johnson, C.L., Mackwell, S.L., Morgan, P., Sandwell D.T., Zuber, M.T., 1997. Lithospheric Mechanics and Dynamics of Venus. In: Bougher, S.W., Hunten, D.M., Phillips, R.J. (Eds.), Venus II, Univ. of Arizona Press, Tucson, pp. 1163–1204.

Phillips, R.J., and 26 colleagues, 2008. Mars north polar deposits: stratigraphy, age, and geodynamical response. Science 320, 1182 - 1185.

Redmond, H.L., King S.D., 2004. A numerical study of a mantle plume beneath the Tharsis Rise: Reconciling dynamic uplift and lithospheric support models. J. Geophys. Res. 109, E09008, doi:10.1029/2003JE002228.

Reese, C., Solomatov, V., Moresi L.-N., 1998. Heat transport efficiency for stagnant lid convection with dislocation viscosity: Application to Mars and Venus. J. Geophys. Res. 103, 13,643–13,657.

Roberts, J.H., Zhong, S.J., 2004. Plume-induced topography and geoid anomalies and their implications for the Tharsis Rise on Mars. J. Geophys. Res. 109, E03009, doi:10.1029/2003JE002226.

Roberts, J.H., Zhong, S.J., 2006. Degree-1 convection in the Martian mantle and the origin of the hemispheric dichotomy, J. Geophys. Res. 111, E06013, doi:10.1029/2005JE002668.

Schmeling, H., Marquart, G., Ruedas, T., 2003. Pressure- and temperature-dependent thermal expansivity and the effect on mantle convection and surface observables. Geophys. J. Int. 154, 224–229.

Scott, D.H. and Tanaka, K.L., 1986. Geological Map of the Western Equatorial Region of Mars

(1:15,000,000). USGS Misc. Inv. Ser. Map I-1802-A.

Simons, M., Solomon, S.C., Hager, B.H., 1997. Localization of gravity and topography: constraints on the tectonics and mantle dynamics of Venus. Geophys. J. Int. 131, 24–44.

Sleep, N.H., Phillips, R.J., 1985. Gravity and lithospheric stress on the terrestrial planets with reference to the Tharsis region of Mars, J. Geophys. Res. 90, 4469–4489.

Smrekar, S.E., Stofan, E.R., Kiefer, W.S., 1997. Large volcanic rises on Venus. In: Bougher, S.W., Hunten, D.M., Phillips, R.J. (Eds.), Venus II, Univ. of Arizona Press, Tucson, pp. 845–878.

Sohl, F., Schubert, G., Spohn, T., 2005. Geophysical constraints on the composition and structure of the Martian interior. J. Geophys. Res. 110, E12008, doi:10.1029/2005JE002520.

Sohl, F., and Spohn, T., 1997. The interior structure of Mars: Implications from SNC meteorites, J. Geophys. Res. 102, 1613–1635.

Solomatov, V.S. and Moresi, L.-N., 1996. Stagnant lid convection on Venus. J. Geophys. Res. 101, 4737–4753.

Stacey, F.D., 1979. Physics of the Earth. John Wiley & Sons, Second Edition.

Steinberger, B.M., 1996. Motion of hotspots and changes of the Earth's rotation axis caused by a convecting mantle. PhD Thesis, Harvard Univ., Cambridge, Mass.

Steinberger, B., 2007. Effect of latent heat release at phase boundaries on flow in the Earth's mantle, phase boundary topography and dynamic topography at the Earth's surface. Phys. Earth Planet. Inter. 164, 2–20.

Steinberger, B., Calderwood, A., 2006. Models of large-scale viscous flow in the Earth's mantle with constraints from mineral physics and surface observations. Geophys. J. Int. 167, 1461–1481.

Steinberger, B., Holme, R., 2002. An explanation for the shape of Earth's gravity spectrum based on viscous mantle flow models. Geophys. Res. Lett. 29, 2019, doi:10.1029/2002GL015476.

Steinberger, B., Holme, R., 2008. Mantle flow models with core-mantle boundary constraints and chemical heterogeneities in the lowermost mantle. J. Geophys. Res. 113, 05403, doi:10.1029/2007JB005080.

Torsvik, T.H., Smethurst, M.A., Burke, K., Steinberger, B., 2006. Large igneous provinces generated from the margins of the large low-velocity provinces in the deep mantle. Geophys. J. Int. 167, 1447–1460.

Turcotte, D. L., Willemann, R.J., Haxby, W.F., Norberry, J., 1981. Role of membrane stresses in the support of planetary topography. J. Geophys. Res. 86, 3951–3959, 1981.

van Thienen, P., Rivoldini, A., Van Hoolst, T., Lognonné, Ph., 2006. A top-down origin for martian mantle plumes, Icarus, 185, 197–210.

Werner, S.C., 2009. The global Martian volcanic evolutionary history, Icarus, 201, 44–68.

Wieczorek, M. A., 2007. The gravity and topography of the terrestrial planets. Treatise on Geophysics, 10, 165–206.

Wieczorek, M.A., Zuber, M.T., 2004. Thickness of the Martian crust: Improved constraints from geoid-to-topography ratios. J. Geophys. Res. 109, E01009, doi: 10.1029/2003JE002153.

Zharkov, V.N., Gudkova, T.V., Molodensky, S.M., 2009. On models of Mars interior and amplitudes of forced nutations 1. The effects of deviation of Mars from its equilibrium state on the flattening of the coremantle boundary Phys. Earth Planet. Inter., 172, 324–334.

Zhong, S.J., 2002. Effects of lithosphere on the long-wavelength gravity anomalies and their implications for the formation of the Tharsis rise on Mars. J. Geophys. Res. 107, 5054, doi:10.1029/2001JE001589.

Table 1: Model parameters. Values in brackets for Earth are for the PREM model, whereas values outside brackets are inferred here. For Mars, values in brackets are for the model with the smaller core radius. E, ν and t_{el} are for the elastic lithosphere model (Mars only).

symbol	parameter	Earth	Venus	Mars
G	gravitational constant	$6.6742 \cdot 10^{-11} \mathrm{m}^3\mathrm{kg}^{-1}\mathrm{s}^{-2}$		
M_0	mass (without atmosphere)	$5.9732 \cdot 10^{24}$ kg	$4.8669 \cdot 10^{24}$ kg	$0.6417 \cdot 10^{24}$ kg
r_0	mean radius	6371.0 km	6051.9 km	3389.5 km
$\bar{C}^0_{2,eq}$	equilibrium	$-479.69 \cdot 10^{-6}$	≈ 0	$805 \cdot 10^{-6}$
$\bar{C}^0_{4,eq}$	coefficients	$1.00 \cdot 10^{-6}$	≈ 0	$2.27 \cdot 10^{-6}$
$\bar{C}^0_{2,ne}$	non-equilibrium	$-4.48 \cdot 10^{-6}$	$-1.97 \cdot 10^{-6}$	$-70 \cdot 10^{-6}$
$\bar{C}^0_{4,ne}$	coefficients	$-0.46 \cdot 10^{-6}$	$0.72 \cdot 10^{-6}$	$2.85 \cdot 10^{-6}$
ρ_0	mean density $M_0/(4\pi/3r_0^3)$	5514.3 kg/m^3	5241.9 kg/m^3	3934.0 kg/m^3
ρ_a	surface atmosphere density	≈ 0	65 kg/m^3	≈ 0
p_a	surface pressure	≈ 0	9.3 MPa	≈ 0
T_a	surface temperature	285 K	740 K	210 K
ρ_c	crust density	2700 (2600-2900) kg/m^3	2950 kg/m^3	2950 kg/m^3
t_c	crust thickness	45 km (22 km)	60 km	50 km
ρ_m	uppermost mantle density	3381 kg/m^3	3378 kg/m^3	3338 (3362) kg/m^3
$t_l = 2d$	lithosphere thickness	100 km	100 km	240 km
r_b	core radius	3480 km	3186 km	1389.5 (1638.5) km
T_b	CMB temperature	3700 K	3500 K	2100 K
E	Young's modulus			$6.5 \cdot 10^{10}$Pa
ν	Poisson's ratio			0.25
t_{el}	Lithosphere elastic thickness			102 km

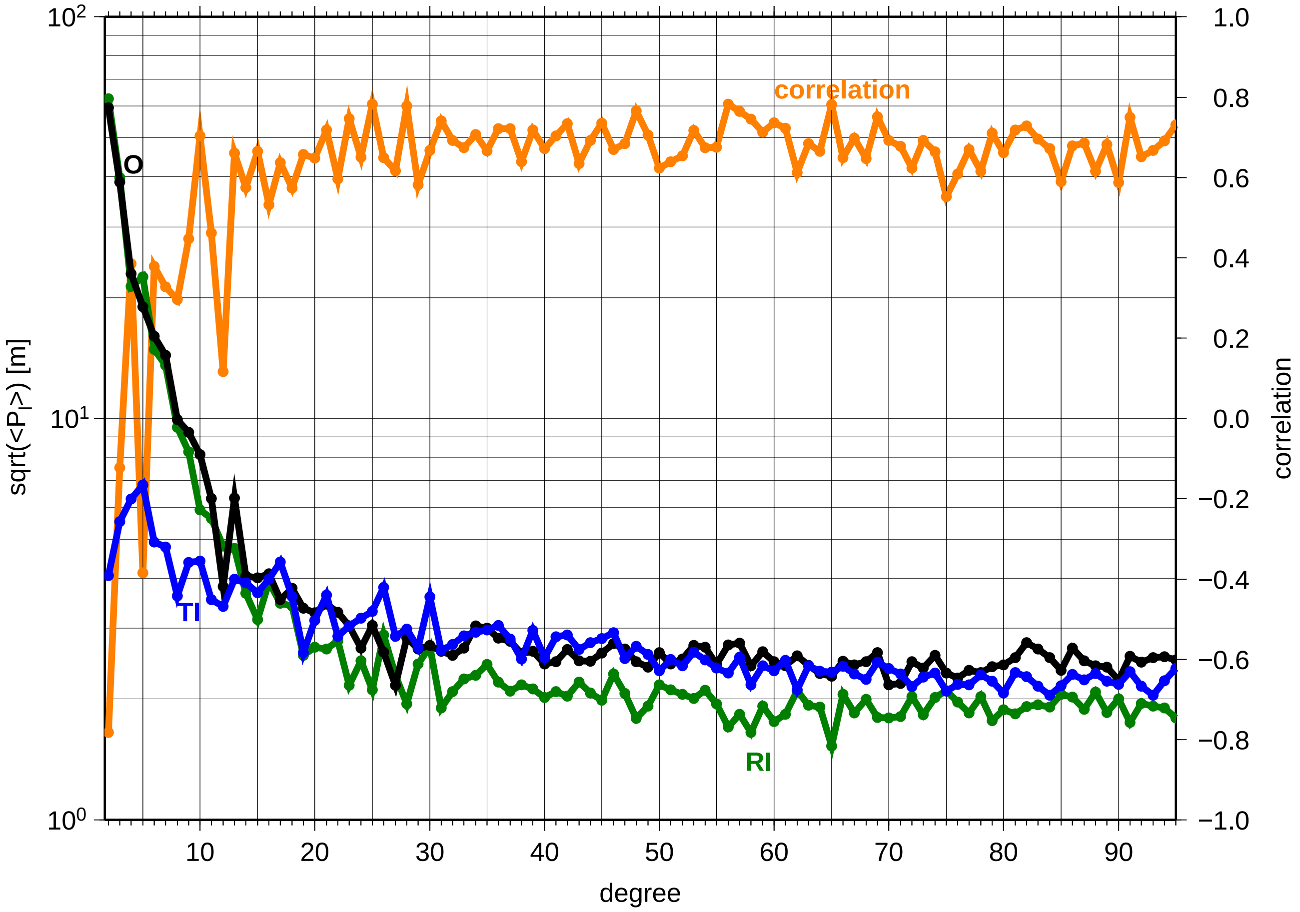

Figure 1: Earth gravity spectrum (square root of power per degree "downward continued" to depth 50 km) and gravity-topography correlation. Line marked **O**: Observed. Line marked **TI**: Modelled with Eq. 2, $t_c = 45$ km and $\rho_c = 2700\text{kg/m}^3$. Line marked **RI**: "Residual" gravity – difference between observed and modelled.

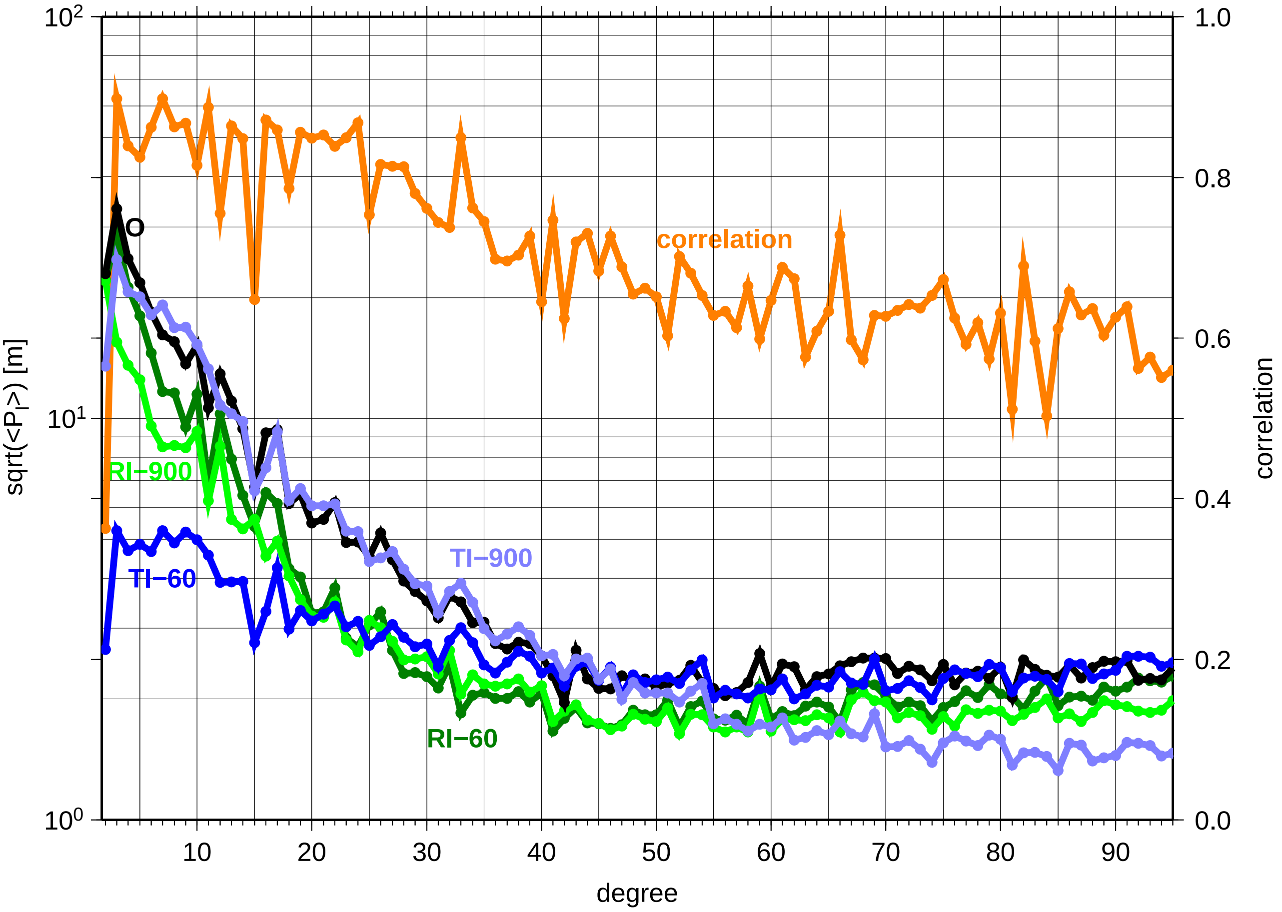

Figure 2: Venus gravity spectrum (square root of power per degree “downward continued” to depth 50 km) and gravity-topography correlation. Line marked **O**: Observed. Line marked **TI-60**: Modelled with Eq. 2, $t_c = 60$ km and $\rho_c - \rho_a = 2.88 \cdot 10^3 \mathrm{kg/m}^3$, line marked **TI-900** with $t_c = 900$ km and $\rho_c - \rho_a = 1.05 \cdot 10^3 \mathrm{kg/m}^3$, Lines marked **RI-60** and **RI-900**: Difference between observed and modelled, corresponding to **TI-60** and **TI-900** respectively.

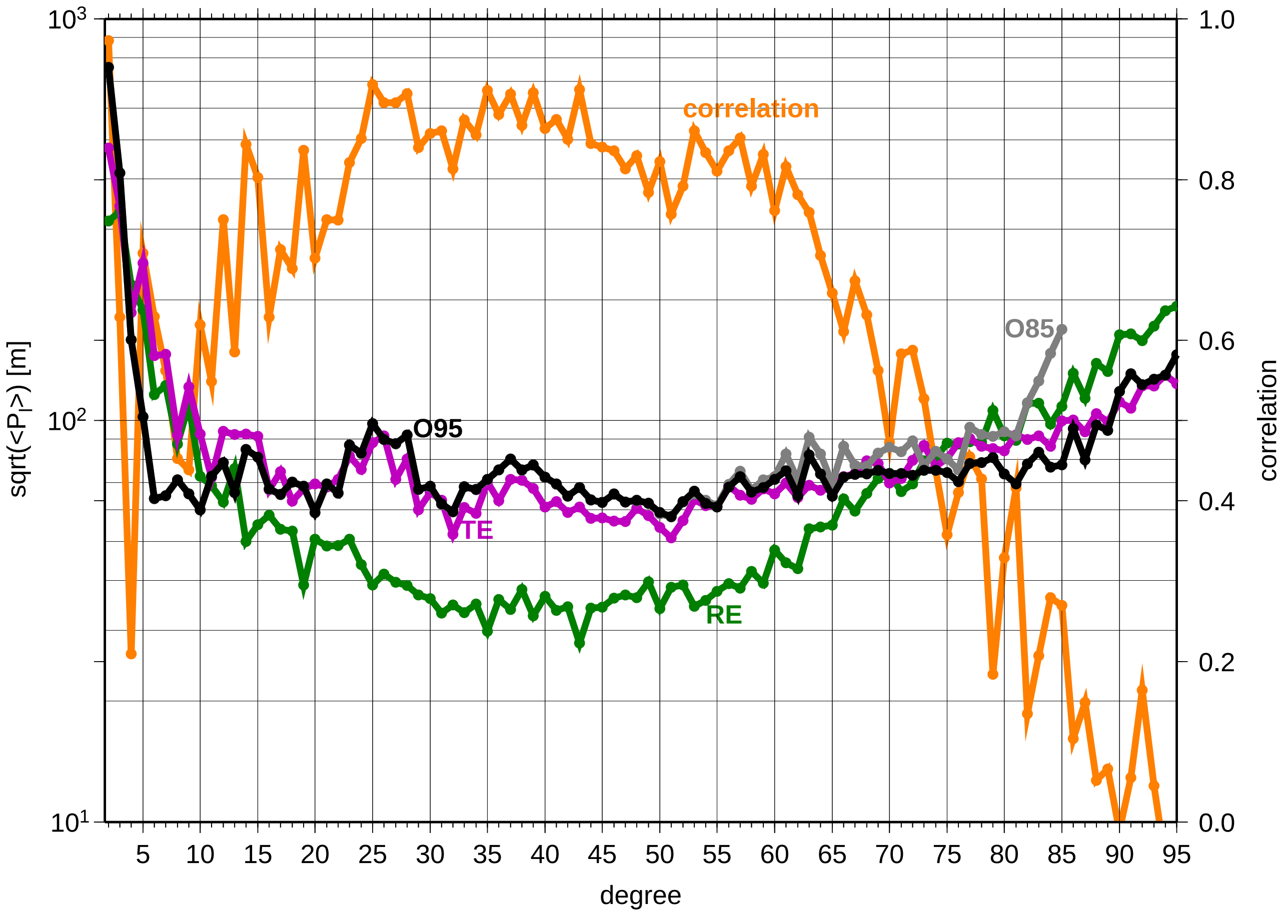

Figure 3: Mars gravity spectrum (square root of power per degree "downward continued" to depth 120 km) and gravity-topography correlation. Lines marked **O95** and **O85**: Observed gravity for models JGM95J01 and JGM85F02. Line marked **TE**: Modelled with Eq. 3, $t_{el} = 102$ km and $\Delta\rho = 2.95 \cdot 10^3 \mathrm{kg/m}^3$. Line marked **RE**: Difference between observed (JGM95J01) and modelled.

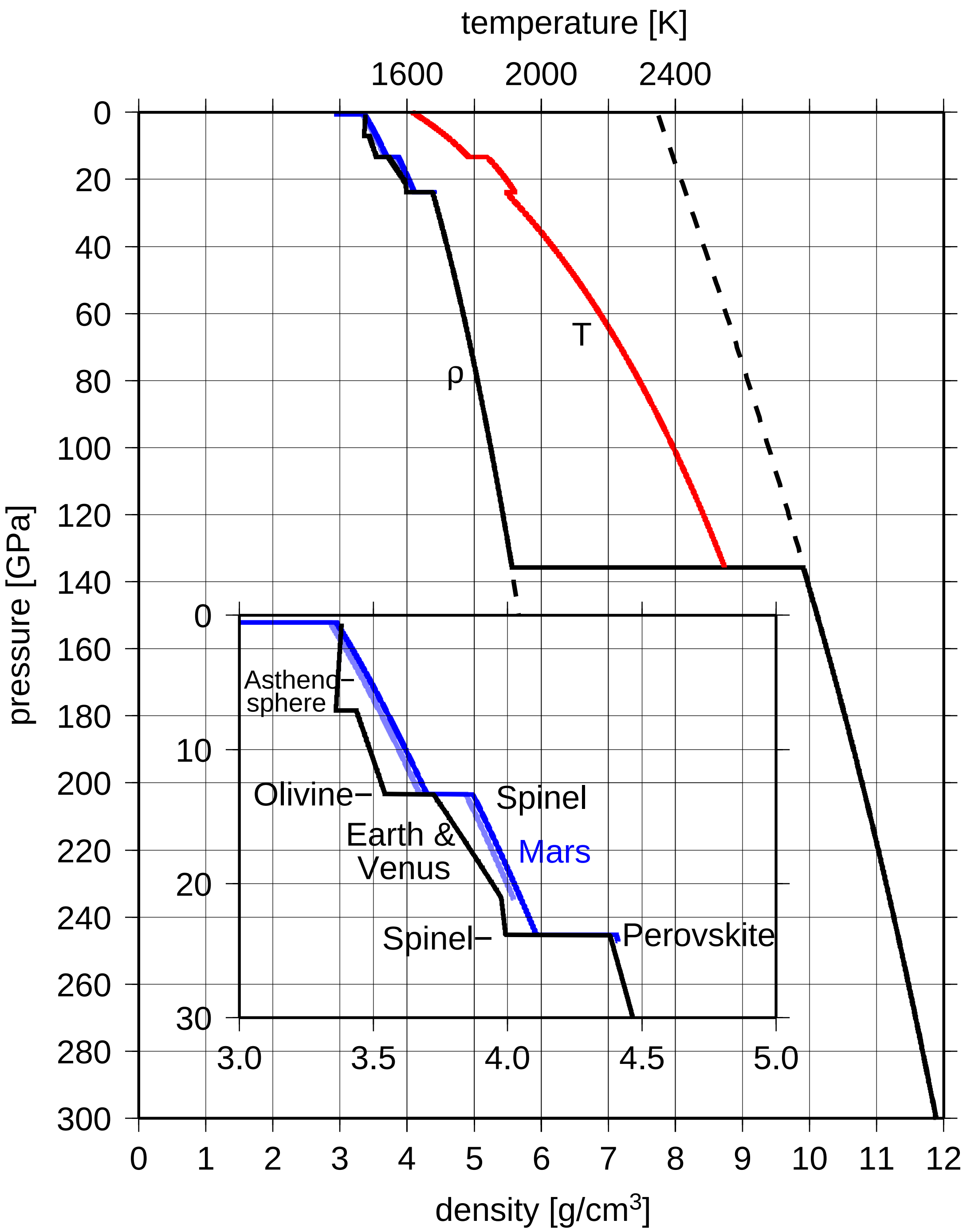

Figure 4: Profiles of density versus pressure inferred from PREM (labeled ρ; Earth & Venus) and self-consistently computed for Mars (two models; dark and light lines) and of adiabatic temperature versus pressure (labelled T; for "Model 2" of Steinberger and Calderwood, 2006). The inset shows a zoom-in of the pressure range for the upper mantles of Earth and Venus and the whole mantle of Mars.

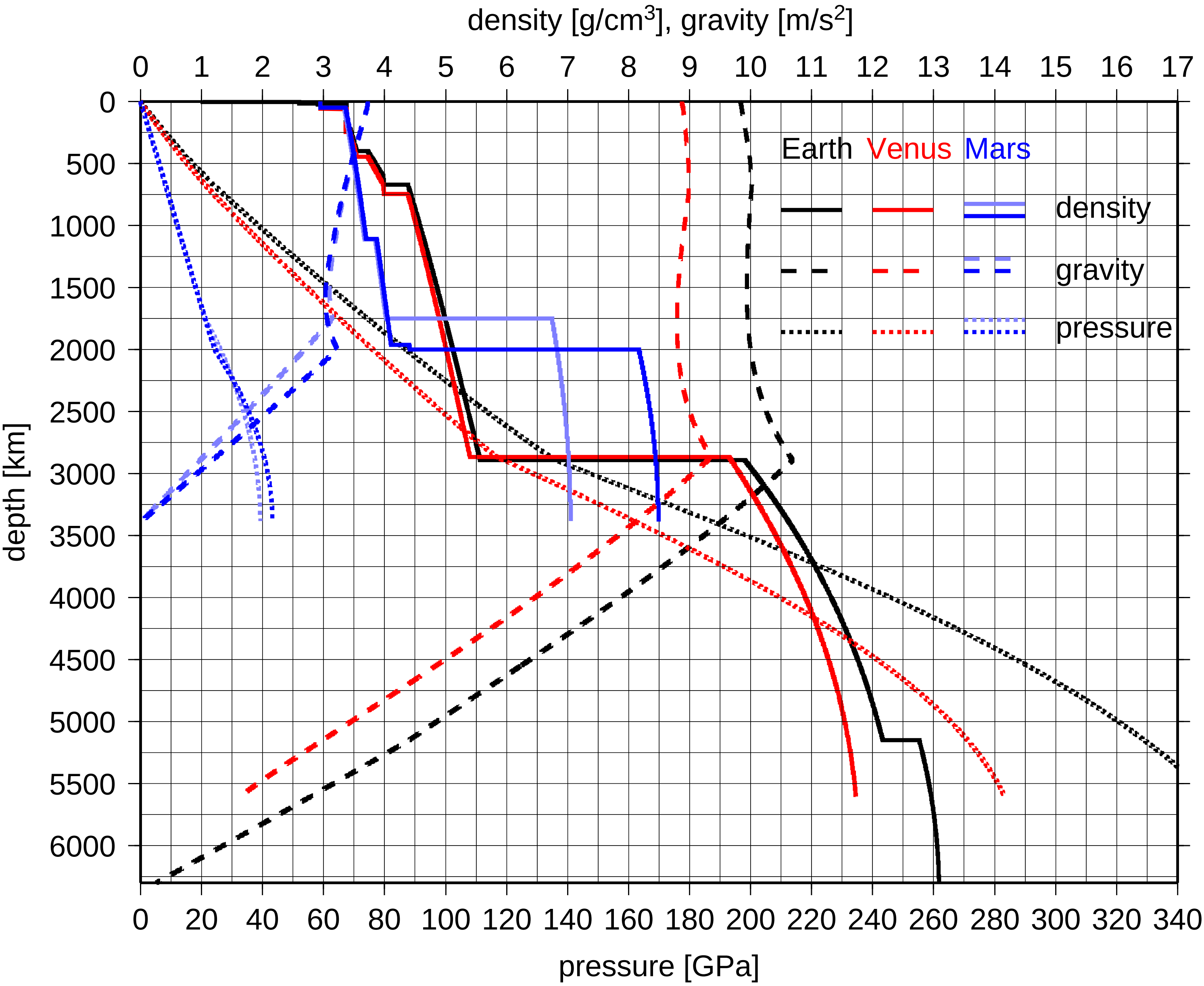

Figure 5: Profiles of density, pressure and gravity for Earth, Venus and Mars (two models).

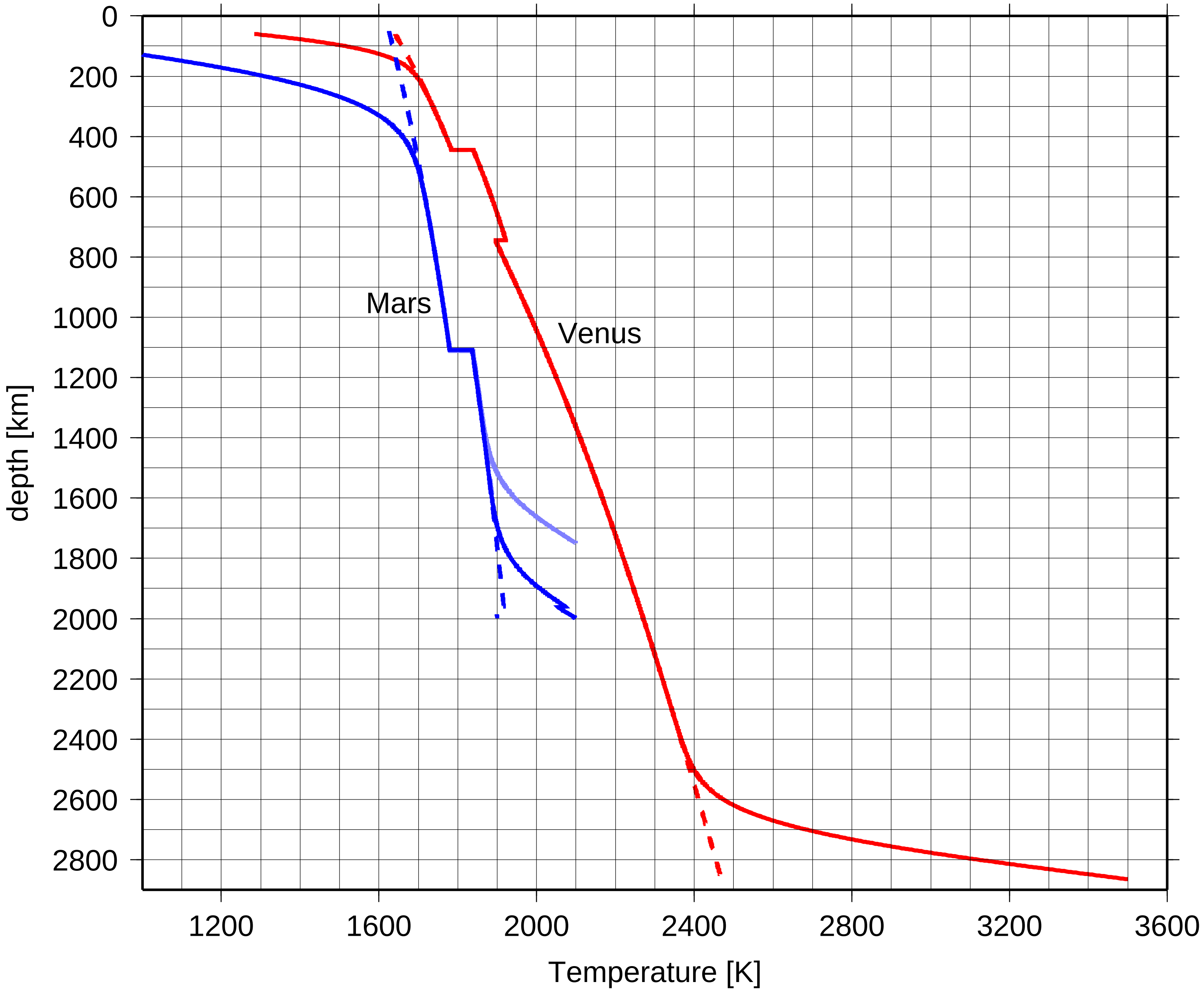

Figure 6: Temperature profiles Venus and Mars (two models). Dashed lines are adiabatic profiles, continuous lines with thermal boundary layers added.

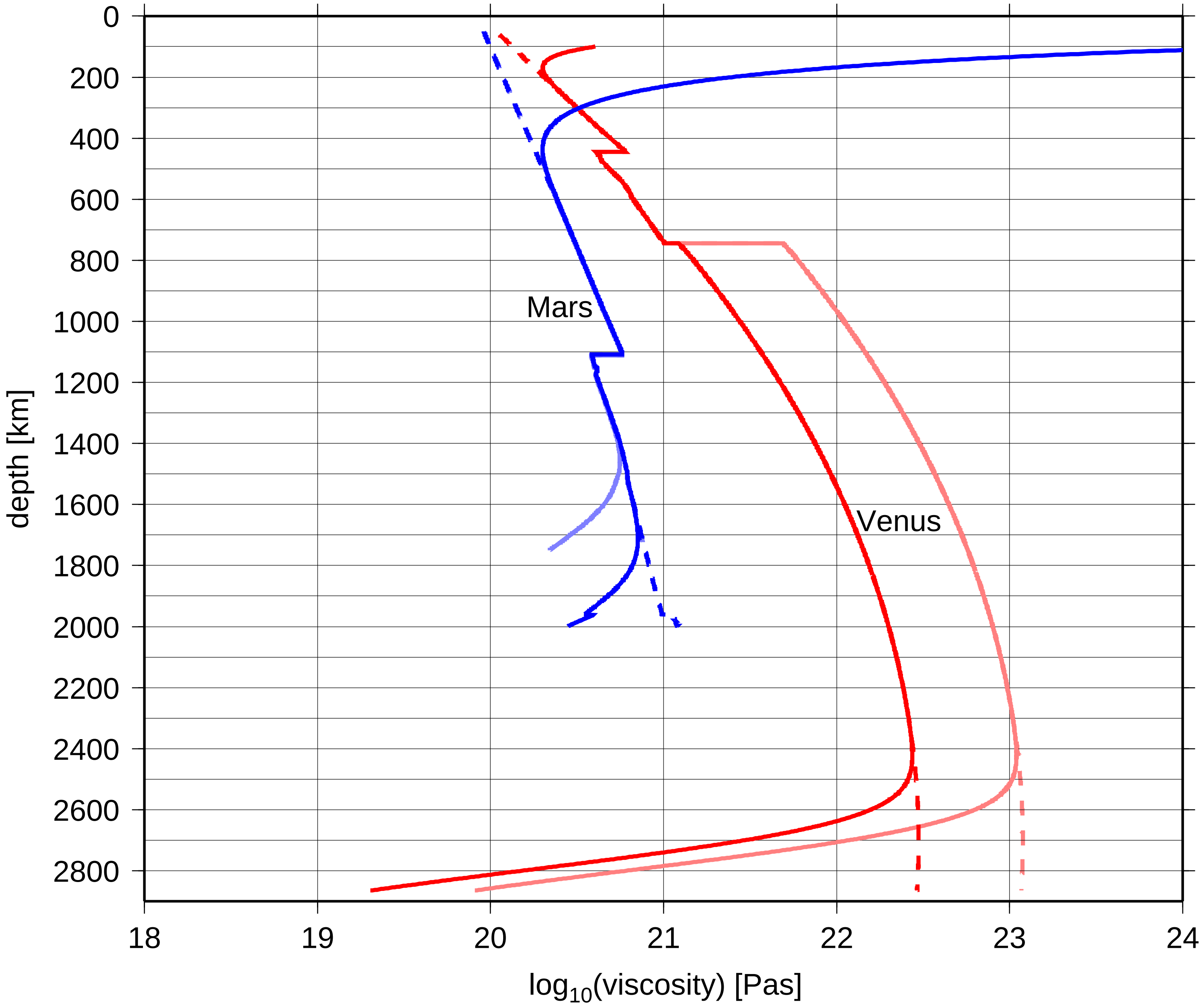

Figure 7: Viscosity profiles corresponding to temperature profiles in Fig. 6. Two cases for viscosity increase across the spinel-perovskite transition of Venus are shown.

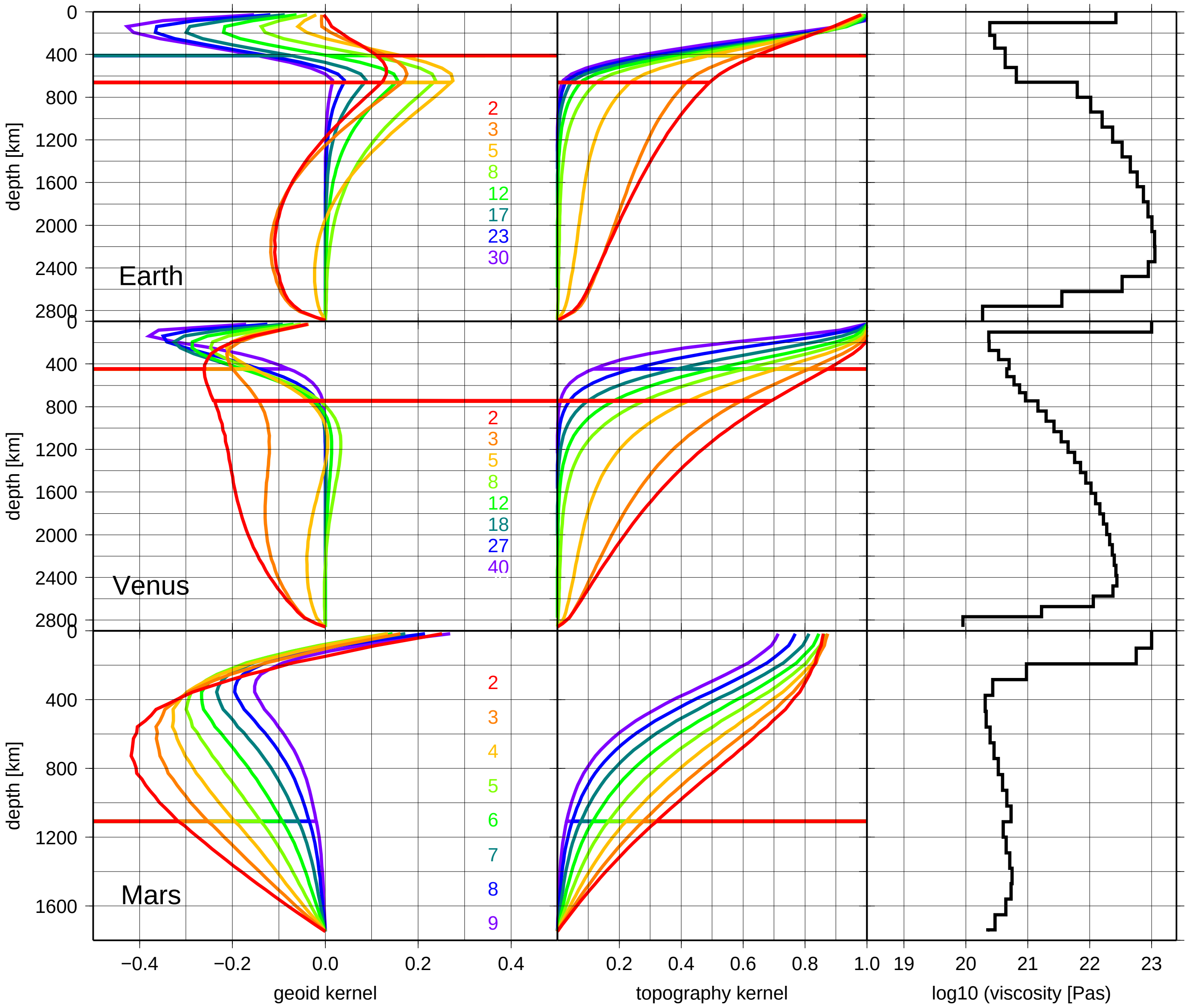

Figure 8: Geoid (left) and topography (center) kernels for viscosity models (right) of Earth, Venus and Mars mantle. Computations for Earth use a stress-free surface. For Venus, the surface is normal-stress-free but with zero horizontal motion. For Mars, zero horizontal motion and vertical stresses corresponding to an elastic lithosphere (see text) are assumed at the surface.

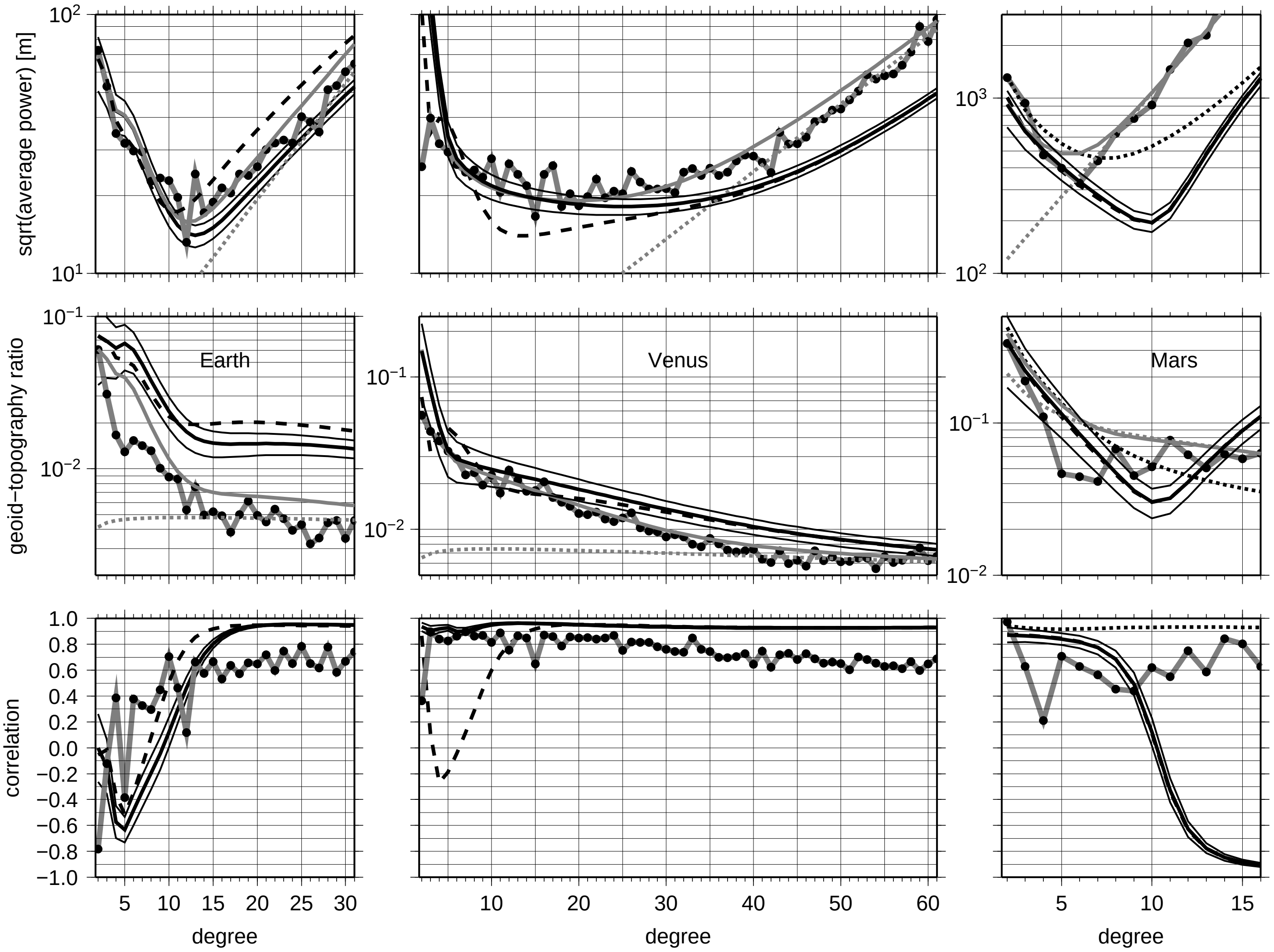

Figure 9: Observed geoid power, geoid-topography ratio and correlation for Earth, Venus and Mars [shaded lines with black dots; as black lines in Figs. 1 – 3] and corresponding predictions from our mantle dynamic models (black lines). Continuous lines are for the same cases as in Fig. 8 (shown with expected uncertainty range, between thinner lines). Additionally predictions for model C of Steinberger and Holme (2008) with lowest viscosity in the transition zone are shown as dashed lines for Earth. The dashed lines for Venus are with viscosity in the lower mantle increased by a factor 4 relative to the other case. For Mars, dashed lines are for the case with smaller core, dotted lines are for the same core radius as continuous lines, but without elastic lithosphere and no horizontal surface velocity (i.e. same upper boundary condition as for Venus). Grey dotted lines are geoid power and geoid-topography ratio for the lithospheric contribution as inferred in section 2 (preferred models), with power corresponding to horizontal lines at $\sqrt{6}$ m in Fig. 1, $\sqrt{5}$ m in Fig. 2, and 70 m in Fig. 3. Grey continuous lines the combination of lithosphere and mantle models. In this case, integration of the mantle contribution in Eqs. 8 and 9 is done only up to the base of the lithosphere (assumed 100 km for Earth and Venus, 240 km for Mars). The power spectra are formally “downward-continued” (to depth 670 km by multiplying values with $[r_0/(r_0-670\text{ km})]^{2l}$ for Earth, 400 km for Venus, 900 km for Mars), such that the range of the vertical axis to be displayed is reduced and the different curves are seen more clearly. The apparent increase of geoid power with degree is a consequence of this display method.

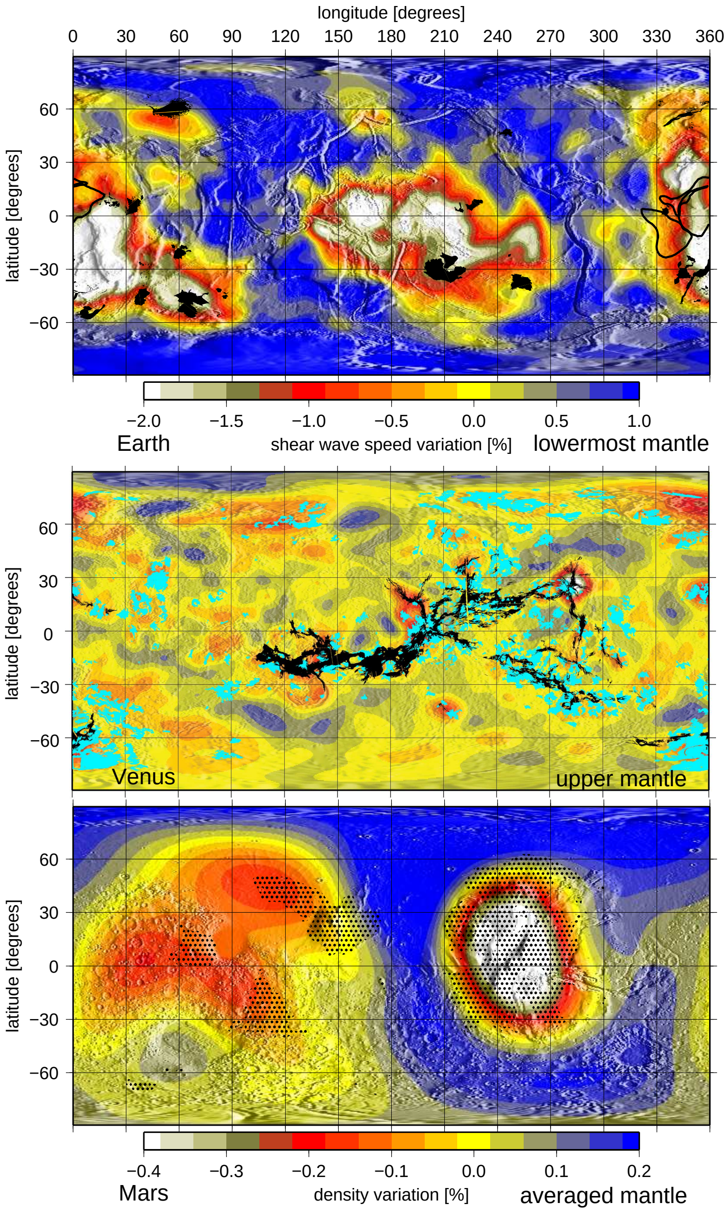

Figure 10: Above: Shear wave speed variations in the Earth's lowermost mantle (*smean* model of Becker and Boschi, 2002) overlain by LIPs reconstructed to their eruption locations (black; for the Central Atlantic Magmatic Province outlines only; after Eldholm and Coffin, 2000; Torsvik et al., 2006; Heeremans et al., 2004). Middle and below: density anomaly models of Venus (essentially upper mantle average) and Mars (whole mantle average) inferred from gravity and the geoid kernels in Fig. 8. On Venus, distribution of rift zones (in black) and Lobate plains from Ivanov (2008) are overlain. On Mars, distribution of volcanics (Scott and Tanaka, 1986; Greeley and Guest, 1987) is overlain in black and partly transparent. Map projections are centered on 180° meridian; shadings indicate topography for orientation.